Design of a Cryogen-Free High Field Dual EPR and DNP Probe

Kan Tagami[1], Raymond Thicklin[1], Sheetal Jain[1], Asif Equbal[1], Miranda Li[1], Toby Zens, Anthony Siaw, Songi Han[1,2]

[1]*Department of Chemistry and Biochemistry, University of California, Santa Barbara, Santa Barbara, California 93106, United States.*

[2]*Department of Chemical Engineering, University of California, Santa Barbara, Santa Barbara, California 93106, United States.*

Abstract

We present the design and construction of a cryogen free, dual electron paramagnetic resonance (EPR) and nuclear magnetic resonance (NMR) probe for novel dynamic nuclear polarization (DNP) experiments and concurrent "in situ" analysis of DNP mechanisms. We focus on the probe design that meets the balance between EPR, NMR, and low temperature performance, while maintaining a high degree of versatility: allowing multi-nuclear NMR detection as well as broadband DNP/EPR excitation/detection. To accomplish high NMR/EPR performance, we implement a novel inductively coupled double resonance NMR circuit (^{1}H-^{13}C) in a solid state probe operating at cryogenic temperatures. The components of the circuit were custom built to provide maximum NMR performance, and the physical layout of this circuit was numerically optimized via magnetic field simulations to allow maximum microwave transmission to the sample for optimal EPR performance. Furthermore this probe is based around a cryogen free gas exchange cryostat and has been designed to allow unlimited experiment times down to 8.5 Kelvin with minimal cost. The affordability of EPR/DNP experiment is an extremely important aspect for broader impact with magnetic resonance measurements. The purpose of this article is to provide as complete information as we have available for others with interest in building a dual DNP/EPR instrument based around a cryogen-free cryostat.

Keywords: DNP, EPR, NMR, Cryogenic

1. Introduction

Over the past few decades Dynamic Nuclear Polarization (DNP) has revolutionized solid state Nuclear Magnetic Resonance (ssNMR) for applications in material and biosolid characterization.[1–3] The success of DNP relies on boosting the inherently low spin polarization of nuclei in a magnetic field by orders of magnitude. DNP works by transferring polarization from suitable unpaired electron sources (of a polarizing agent–PA) to adjacent NMR nuclei of interest via the irradiation of electron paramagnetic (EPR) transitions that either alters the electron spin polarization of electron spins coupled to the nuclear spins or drives simultaneous electron-nuclear spin transitions. This process can theoretically lead to 660 fold signal enhancements for protons, and even more for other nuclei. The massive boost in NMR signal induced by DNP provides a multitude of benefits including but not limited to: studies of low natural abundance nuclei without expensive enrichment; shortened experimental times by factors of hundreds of thousands; and selective surface studies of dilute species.[4–8]

However, DNP has yet to reach its full potential due to incomplete knowledge of the electron-nuclear spin system, further aggravated by DNP's decreasing efficiency at high fields over 14 Tesla.[9,10] Hence, DNP studies can be critically enhanced with diagnostic tools to evaluate the spectral and spin dynamics of both the nuclei and electrons in the sample system under DNP conditions. It has been shown that electron spin lattice relaxation time (T_{1e}), the g anisotropy, electron-electron couplings, electron spectral diffusion and nuclear spin diffusion all play critical roles in tuning the DNP efficiency.[11,12] Studies often evaluate these parameters with pulsed EPR at X or Q band, i.e. lower magnetic fields, but many of the relevant EPR parameters are either field dependent or difficult to resolve at lower magnetic fields. Thus, an accurate assessment of DNP parameters requires dual NMR and EPR detection capabilities under DNP conditions to characterize spin dynamical properties of samples containing the same PA concentration and solvent, subjected to the same microwave irradiation power, cryogenic temperature and magnetic field. To fulfill these requirements a dual EPR/DNP probe with simultaneous pulsed EPR and NMR capabilities are needed.

While dual EPR/DNP probes would be critical tools for DNP studies, only a handful of such diagnostic instruments exist. Some currently existing cryogenic high field ($> 3T$) EPR/DNP probes include a dissolution DNP system from Kockenberger et. al at 3.35T,[13,14], the Griffin group at 5T,[15] the Goldfarb group at 3.35T[16], and the Han lab at 7T[17]. An important bottleneck is the lack of commercial availability of dual EPR/NMR probes and spectrometers, as well as the limited availability of high field EPR hardware components including solid state microwave (μw) sources, amplifiers and receiver systems sensitive enough to detect EPR signal. Most commercial DNP systems are powered by a gyrotron due to the need of high power in the 10s of watts range. However, it is non-trivial to achieve

Email address: songi@chem.ucsb.edu (Songi Han[1,2])

quick pulsing/gating and phase cycling of the radiation using a high power μw source.[18] In theory, any DNP probe can be adapted for EPR detection. However, the probe should be simultaneously optimized for NMR radio frequency (RF) receive and transmit and μw receive and transmit, as well as for minimized μw reflection at the EPR frequency. Most DNP (in particular MAS) probes are only optimized for transmitting a single polarization of μw irradiation, which limits their applicability for the highly sensitive induction mode EPR detection (i.e detection of μw emission with orthogonal polarization to the excitation).[19] However, even in a static DNP setup, it is nontrivial to achieve optimal NMR and pulse EPR detection with high fidelity at high magnetic fields.

2. Methods: Design Considerations

In this paper we will outline design considerations for the construction and performance of a dual EPR/DNP instrument and probe, designed to work with a solid state μw source generating moderate power (10s to 100s of mW) and at cryogenic temperatures down to liquid helium temperatures. The design of the probe is focused around simultaneously optimizing three main aspects: 1) efficient cooling of the sample to cryogenic temperatures; 2) robust, sensitive and versatile NMR circuit for receive and transmit; and 3) efficient μw transmission and reflection for optimal EPR (and by extension DNP) performance.

2.1. Thermal Design Considerations

Temperature performance is critical for the operation of a DNP/EPR probe. Typically, lower temperatures will yield larger Boltzmann polarization, more impressive DNP enhancements,[1] and offer access to slower dynamics that permit DNP and cross polarization transfer to methyl groups (which freely rotate at typical DNP temperatures of ~100K).[20–24] Furthermore, MAS using cold nitrogen gas is limited in the achievable spinning frequency, while cold helium gas has fluid dynamical properties similar to air and hence can be used to achieve much higher MAS frequencies.[23,25–28] Hence, performing DNP at temperatures lower than liquid nitrogen (77K) is of great interest to the magnetic resonance community. To achieve these temperatures, the right choice of cryostat must be made, followed by adequate thermal design of the probe. Practical factors must be also considered when deciding on the design of a cryostat, including cost, cooling time, freeze quench (i.e rapid cooling) capability, and available space.

There are a variety of cryostat designs used for DNP/EPR spectrometers; but they can be roughly broken down into 3 categories: closed cycle cryostats, bath cryostats, and continuous flow crysotats.[29–32] *Bath cryostats* are essentially a specialized dewar containing liquid helium or nitrogen in which the sample or cold finger is placed. The sample is cooled by thermal contact with the cyrogenic liquid or cold finger. These cryostats can hold very low temperatures (~ 4K) for long experimental times, and can cool large sample volumes (such as the coils of superconducting magnets). However, these cryostats are not optimal for achieving thermal cycling or variable temperatures, but have nonetheless been used effectively in dissolution DNP setups.[33,34] *Continuous flow* cryostats use the latent heat of vaporization from boiling helium to cool a cold finger, and subsequently the sample. The boiling helium is constantly replaced from an external dewar (hence continuous flow), while the boiled off helium is allowed to escape the cryostat. This method consumes the most cryogens, but can easily reach a wide range of temperatures of $> 4K - 300K$, and can be thermally cycled quickly and easily. Additionally, these cryostats become more efficient for small sample volumes such as those used in DNP. Many high field EPR/DNP probes have used this style of cryostat effectively (such as the Oxford Spectrostat or Janis SuperTrans),[13,15,16,35–37] including the cryostat that was previously used in the Han lab to achieve dual EPR and DNP transmit and receive.[38] *Closed cycle cryostats* use a mechanical compressor to cool a cold finger to cryogenic temperatures. This cold finger can subsequently cool a sample chamber via thermal contact with an exchange gas or can cool a supply of helium gas which can then flow over the sample chamber. These cryostats have much less overall cooling power, and tend to cool down much more slowly when compared to bath or continuous flow cryostats. Therefore they require more careful thermal design of the DNP/EPR probe to reach their minimum and desired temperatures. The benefit of these cryostats is that they can readily achieve temperatures below ~4K, continuously and without the need for continuous replenishing of the cryogens. This makes them ideal for long experiment times or experiment runs requiring multiple samples. These cryostats are becoming more popular due to the rising cost of liquid helium, and a number of NMR/DNP/EPR systems exist that rely on such cryostats.[23,33,39–41] We should note that there exists another type of cryostat known as a "stinger" system, which combines a closed cycle helium system with a bath or continuous flow cryostat. In these systems the helium evaporates from a bath or a flow cryostat and is recaptured and re-condensed.

2.1.1. Thermal Design of Probe

In most cases, cryostats are purchased commercially (often custom commissioned), leaving the user or developer with the need to come up with a thermal design for the DNP/EPR probe. The thermal design of the probe is crucial for optimizing the temperature performance that relies on minimizing heat exchange with the ambient environment. The two dominant mechanisms of unwanted heating are thermal conduction along temperature gradients in the probe, and blackbody radiation emitted and absorbed from non-reflective surfaces of the probe or cryostat.[42]

Thermal conduction is dictated by the shape and materials that compose the probe. Heat transfer can be minimized by constructing the probe out of low thermal conductivity materials such as fluoropolymers (e.g. PTFE,KEL-F), G-10 fiberglass, carbon fiber or stainless steel; instead of high thermal conductivity materials such as copper and aluminum. The thermal conductivity of some cryogenic materials is shown in section 1.1 of the SI. Furthermore, material shapes with a higher cross section (across a thermal gradient) will conduct more heat, and

thus thin structures are preferred. These materials must also maintain structural stability at cryogenic temperatures (i.e not become too brittle) and have matched coefficients of thermal expansion to avoid structural failure, while the structure of the probe must be strong enough to support its own weight. Furthermore, material selection and shape must be balanced with other requirements for the probe such as RF and μw transmission. The RF transmission lines must be conductive enough to efficiently transmit RF, which means constructing them out of highly (electrically) conductive materials such as copper and/or making them thicker, which directly contradicts the design for minimizing thermal conduction. The μw waveguide must also be made out of a conductive material and be wide enough to support the desired μw transmission mode (i.e the hybrid HE_{11} mode for efficient coupling to a free space gaussian beam). Unfortunately, good electrical conductors are also generally good thermal conductors. However, the conductivity and geometrical requirements of the waveguide can be relaxed by plating a thin layer of electrically conductive material on a less thermally conductive material such as stainless steel. At the desired high RF and μw frequencies, the skin effect makes a thin conductive layer ($\sim 20\mu m$ for 300MHz) sufficient for maximum RF transmission and electrical conductivity. Besides thermal conduction through solid material, gas filled cryostats must contend with undesired heat transfer through the helium gas present in the cryostat. This effect can be mitigated by confining the cooled helium gas to a small area containing the cold finger and sample, e.g. by adding baffles that restrict gas flow.

Thermal radiation is another mechanism of heat transfer that can be crucial in achieving ultra-low temperature DNP/EPR operation. This mechanism occurs because surfaces emit and absorb electromagnetic radiation based on their temperature (i.e black body radiation). Thus, care must be taken to reduce radiation absorbed by cold parts of the probe, such as the RF probehead. One way to reduce the emission and absorbance of radiation is to construct the probe from reflective, low emission materials, such as polished metals. Another method is to physically block/absorb radiation from the source before it reaches colder parts of the probe. This can be accomplished through radiation shields such as baffles or multilayer insulation. Notably, materials at a lower temperature emit far less radiation, and thus radiation shields which are cooled to lower temperatures perform better.

2.2. RF Performance Design

RF performance stability dictates the usefulness of the probe for both NMR and DNP applications, but is perhaps the most difficult part to design due to space constraints imposed by the cooling setup and the μw waveguide. There are a myriad of factors that determine NMR performance, stability and applicability including B_0 homogeneity, B_1 homogeneity, RF Power handling, nutation frequency, sample filling factor, circuit filling factor, Q factor, isolation, tuning range and tuning mechanism. A comprehensive review of all the factors that go into designing an ideal NMR RF probe is beyond the scope of this paper and can be found elsewhere.[43–46] However in short, the two main measures of performance for a solid state NMR probehead are a strong RF B_1 field (i.e nutation) and large signal to noise ratio (s/n). In general, the B_1 has the following dependence:[44]

$$B_1 \propto \sqrt{P_{RMS}\eta_{CFF}Q_T}, \tag{1}$$

where P_{RMS} is the RMS power (in watts) delivered to the circuit, η_{CFF} is the circuit filling factor (i.e the percent of RF energy that is stored in the sample coil and Q_T is the (unmatched) quality factor (see SI section 2.2). The Q_T is related to the resistance of the circuit components, where a higher Q means less RF energy lost to heat. The probehead factors that affect s/n are:[44]

$$s/n \propto \sqrt{\eta_{CFF}\eta_S Q_T}, \tag{2}$$

where η_S is the sample filling factor which is the fraction of the magnetic field generated by the sample coil that intersects with the sample. Thus to maximize NMR performance, P_{RMS}, η_{CFF}, Q_T and η_S must be considered in the RF design, along with other practical factors, such as the ease of tuning/matching and the tuning bandwidth.

2.2.1. RF Circuit Design

A variety of RF circuits (both double and single resonance) have been used for cryogenic solid state DNP applications including transmission line circuits,[15,16,47,48] and cryogenically tuned circuits,[17,23,35,49]. The choice of circuit design will impact η_{CFF}, P_{RMS}, Q_T, and the practical utility of the probe.

Transmission line circuits have the tuning and matching elements of the RF circuit far from the sample outside the cryostat. These circuits connect to the NMR sample coil via coaxial lines that are pruned to a specified length (generally a multiple of $\lambda/2$) that provides the necessary distributed capacitance and inductance to give resonance at a specified frequency, while still being the correct length to reach the sample from outside the cryostat.[32,50] Fine tuning and matching capacitors are placed outside the cryostat/magnet, and are connected to the sample coil via the coaxial lines. These circuits have higher power handling (allowing higher P_{RMS}) due to the high power handling of coaxial cables and large externally mounted variable capacitors. Furthermore the variable capacitors are placed outside the cryostat at room temperature, making adjustments easier, freeing up precious space in the cryostat, and allowing the use of non-cryogenics rated, variable, capacitors. However, the reliance on frequency-specific length of the transmission line means that the tuning bandwidth is often limited to a single nuclei per channel. Furthermore, transmission line circuits can have lower Q and η_{CFF} due to the use of long (slightly lossy) transmission lines as resonant components, while larger diameter (higher Q) transmission lines can conduct more heat into the probe.[32,51]

Cryogenically tuned circuits[23,29,35] are generally based on discrete lumped element inductors and capacitors rather than transmission lines (not to be confused with cryogenically cooled circuits which are still external to the cryostat[52]). These circuits have all the tuning and matching elements inside the cryostat near the sample. These probes have the advantage of

achieving a wide tuning range (depending on the variable capacitors used), higher Q due to cryogenic cooling of the resonant circuit elements[52], and a higher η_{CFF} because energy is not stored in the inductance of the coaxial lines. However, the discrete tuning elements take up a large amount of space in the cryostat, mechanical tuning of capacitors can become challenging at cryogenic temperatures (although commercial capacitors exist which can handle cryogenic conditions), and the helium atmosphere in the cryostat causes capacitors to be more prone to arcing at high RF power (though this problem is partially mitigated at low temperatures).[32,53]

Matching the circuit to the input impedance of the RF signal is another design aspect that must be considered. This matching can either be done capacitively or inductively. To date, most solid state cryogenic NMR and DNP probes have used capacitive coupling.[23,35,49] We have previously suggested that an inductively matched circuit can provide benefits over capacitive matching for cryogenic DNP NMR.[54] Inductively matched probes are inherently balanced without additional components, which eliminates ground loops, reduces dielectric losses between the resonant circuit and ground, and reduces noise interference from outside sources.[55,56] Furthermore, it has recently been shown that inductive matching can offer higher η_{CFF} for multi resonant probes.[57]

2.2.2. *Circuit Components*

Once a circuit layout is chosen the next step is to choose the components necessary to physically build the circuit, including the capacitors and inductors.

Capacitors are a crucial component to any NMR probe, as the ability to tune and match are essential for maximizing B_1 and s/n at a desired frequency. For a solid-state NMR probe, the most important factor for these capacitors are their power handling (which determines the maximum P_{RMS}).[45] Other major concerns include the mechanical and electrical robustness of the variable capacitors under thermal cycling between room temperature and liquid helium temperatures, and the physical size (with larger capacitors having larger parasitic inductance). Most probes use a combination of fixed capacitors and variable capacitors. Fixed capacitors can be made to have favourable mechanical properties (i.e robustness and small size) and electrical properties (i.e high voltage handling and low resistance), but dont provide the flexibility to make the small adjustments to tuning and matching necessary for resonant probes, which necessitates the incorporation of variable capacitors.

Fixed capacitors are generally commercially available non-magnetic NPO/C0G ceramic chip capacitors with a capacitance of around one to a few hundred picofarad (pF), a (DC) voltage rating of up to a few kV, and a Q of a few hundred to a few thousand. A more in-depth review of fixed capacitors for NMR is available elsewhere.[45]

The selection of variable capacitors is more challenging as they need to be variable within the desired range (often $\sim$ 1 - 10s or 100s of pF), and have a tuning mechanism that may not be robust enough to survive hundreds to thousands of thermal cycles between cryogenic and room temperatures. Commercial capacitors exist that can handle cryogenic temperatures,[49,58] but they tend to be very large in size relative to the space available in the cryostat and costly. Our own experience with commercially available variable capacitors has shown they can be mechanically unreliable when subject to extreme temperatures and thermal cycling for prolonged times; however other groups have successfully built cryogenic probes using commercially available variable capacitors from companies such as Voltronics.[29,32,59,60]

RF Coils are the most important part of a typical NMR spectrometer as they generate the magnetic field necessary to interact with the nuclear spins. Good NMR coils will have low resistance/high Q (which affects the overall Q_T of the circuit), high η_s along with low electric fields at the sample, and high magnetic field homogeneity to achieve maximum s/n and high B_1. To date, non-spinning solid state DNP probes have made use of solenoids,[15,47,49] saddle (Helmholtz) coils,[16,17,61,62] and Alderman-Grant (AG) coils[17]. Traditionally, solid state NMR probes use solenoids as sample coils due to their high Q and high η_s.[45] However, the axial nature of these coils mean μw's transmitted down the length of the magnet must pass through the winding of the solenoid coil to reach the sample, which can attenuate the incident μw power. Furthermore, the sample exchange mechanism of our probe requires the sample to be removed vertically (parallel to B_0) rather than horizontally. This can be achieved with saddle coils that also provide good magnetic field homogeneity, and hence have been used extensively in DNP probes. AG coils show similar B_1 homogeneity to saddle coils, and are a type of slotted cylinder resonator that is tuned with capacitors in series.[63] The series tuning increases the operating frequency of the coil readily to the ^{1}H NMR frequency range at high magnetic fields and reduces the overall voltage across the coil, resulting in less dielectric loss and sample heating.[55] However the low overall inductance of AG coils leads to difficulty tuning to lower frequencies $<$ 100 MHz, and often decreased RF efficiency due to parasitic inductance.

The auxiliary coils are a necessary component to generate multiple resonances in a multi-frequency tuned circuit. They are also important components of the circuit as they can affect Q and η_{CFF}. For most double resonant circuit designs, a higher value of inductance for the auxiliary coil will result in a higher H channel η_{CFF} and a lower X channel η_{CFF}. Good auxiliary coils will have as high a Q as possible, as small parasitic capacitance as possible (high self resonant frequency), and be easy to magnetically couple to (in the case of inductively coupled circuits). Solenoids are a good choice because they provide the highest Q for a given inductance, and are also fairly easy to magnetically couple to. Additionally, care must be taken that the lead lengths connecting the coil to other components are accounted for when measuring the inductance of the coil, given that long leads can add inductance, resulting in a different balance of η_{CFF} in the RF circuit than expected.

2.3. *μw Design*

The design to achieve optimal μw transmission is critical to both the EPR and DNP performance of the probe. Maximum μw power at the sample ensures large μw B_1 which contributes

to enhanced DNP performance, especially at higher temperatures where faster T_{1e} relaxation counteracts μw-driven saturation or simultaneous electron-nuclear spin transitions. Furthermore, maximizing the μw power transmitted to and from the sample enhances the EPR signal to noise ratio (s/n).

Strategies to maximize the μw power in the probe itself (discounting μw sources, quasi optics, ect. outside the probe) can be broken down into 2 parts: to optimize μw transmission through the probe to the sample and to optimize the μw properties of the sample holder. These two aspects will be discussed next.

2.3.1. μw Transmission

At high frequencies transmission lines become very lossy due to the skin depth effect. Thus traditional methods of 2 conductor electromagnetic propagation using coaxial lines become extremely inefficient for long transmission distances, such as the length of the EPR/DNP probe (spanning~1 m). In EPR probes, coaxial lines for μw transmission are only used up to Q band (~45 GHz). Most EPR and DNP spectrometers rely on waveguides for μw transmission. Low field (X and Q band) and early high field ($\geq$ W band) systems relied on metallic **rectangular waveguides** to transmit μw's in the fundamental TE_{10} mode. However, the dimensions of these waveguides is on the order of the wavelength of the desired frequency, and thus become very small at high fields/frequencies. Additionally, the decrease in waveguide size paired with the skin effect leads to more losses in the wall of the waveguide (although not as much as in coaxial lines).[64] This problem was overcome when the Freed group developed the first **quasi-optical** high field EPR probe operating at 250 GHz.[65] This probe relied on a μw beam propagating in free space (in a fundamental gaussian TEM_{00} mode) instead of confining the beam inside a conventional single mode waveguide. This design has the advantage of no conductor losses, and can achieve a transmission loss of ~1.5dB/m at 250GHz, which is much less than the loss with traditional rectangular (TE/TM mode) waveguides. However for long transmission distances at high frequency, this approach requires refocusing of the gaussian beam using components that are either large (mirrors) and/or are lossy/reflective (teflon dielectric lenses). Additionally it requires precise alignment of optics, and the beam cannot be turned or tapered without additional large, precise quasi optical components (mirrors and lenses), which can be problematic in the limited space of a dual DNP/EPR probe/cryostat. **Corrugated waveguides** were first introduced in EPR probes by Smith et. al to achieve optimal coupling through the cryostat to the sample with minimal losses of <0.01dB/m at 200 GHz,[66] and were later implemented in gyrotron-based DNP systems by Woskov et. al (~0.3dB/m loss at 250 GHz).[67] These oversized, cylindrical waveguides support the hybrid HE_{11} mode which is very similar to the fundamental Gaussian TEM_{00} mode, which allows low loss transmission (due to minimal current on the metallic walls), as well as good coupling to Gaussian beams such as those propagated through quasi optics, and can thus be easily paired with a quasi optical detection/pulse forming stage. Additionally, these waveguides generally require a smaller diameter than quasi-optics and can be tapered to focus μw power on a small sample volume. These advantages have led corrugated waveguides to become the de-facto standard for μw transmission in high field DNP and EPR probes. However, corrugated waveguides are often one of the most expensive components of the EPR probe as they require a complex manufacturing process. Recently, evidence has been presented that cheaper, smooth walled, cylindrical waveguides could also be effective for DNP μw transmission,[49,68] but losses associated with mode conversion make them non-ideal for EPR detection.

2.3.2. μw Properties of Sample Holder

An equally important aspect of μw design for a high field EPR/DNP probe is the sample holder. The sample holder must have favourable μw and RF properties to allow both types of irradiation to effectively transmit to the sample.

Many EPR probes have the sample inside a μw resonator to increase the μw $B-1$ field experienced by the sample. However, these resonant structures must be compatible with concurrent RF penetration to the sample for NMR detection. To date, a number of DNP resonators have been introduced, including single mode TE_{01} resonators,[69] fabry-perot (FP) type resonators,[70,71] and a newly introduced photonic bandgap resonator.[61] Most *single mode* cavities for DNP follow the design of Weis et. al,[69] which uses a flat helical coil as the main body of the resonator and as the NMR coil. The dimensions of single mode cavities must be on the order of the wavelength of the desired frequency, and hence at higher frequencies the dimensions become smaller and much harder to machine to tolerance. This small size also leads to low sample volumes, which can reduce both the EPR and NMR sensitivity (3nL at 260 GHz)[72]. Additionally, the skin depth effect paired with the small size creates resistive losses in the sample cup, leading to a lower quality factor "Q" (analogous to the NMR circuit Q). The single mode design also does not allow for induction mode EPR detection (only reflection mode), which can result in lower s/n.[73]

Fabry Perot (FP) type resonators are essentially two reflectors spaced at a distance from each other such that a standing wave forms between them at a certain frequency. FP's can be larger than the wavelength, and have already been shown to work for solution state DNP setups at 260 GHz,[70], and a low Q standing wave structure has been used for cryogenic solid state DNP/EPR experiments at 140 GHz[16]. However, FP resonators have "nodes" of alternative magnetic and electric fields, and thus care must be taken such that the sample is only in the magnetic field node to avoid sample heating, and to maximize μw B_1 homogeneity. Therefore the sample volume is often still very small, with the maximum reported so far of 90 nL at 260 GHz.[74]

Recently a resonator based on a 1D *photonic band gap structure* has been developed by Nevzorov et. al.[61] This resonator consists of an alternating stack of dielectric disks between two reflective surfaces. Here, a standing wave pattern is formed similar as in a traditional FP resonator, except that the sample can be placed in each node (i.e between each disk) which allows for larger sample volumes, demonstrated with the use of 2.5μL of samples by Nevzorov and coworkers.

With all resonators, sample volumes remain small, and the precise mechanisms needed to tune the resonators often present a problem, especially when space inside the magnet bore is at a premium. Additionally, precise mechanical tuning at cryogenic temperatures, while possible, presents a costly design challenge. Furthermore, high Q cavities have an inherently narrow bandwidth, and thus need to be re-tuned for each μw frequency, which renders frequency swept experiments very challenging. To perform multi-frequency experiments such as ELDOR, the Q of the resonator must be somehow reduced to give an appropriate bandwidth or a double resonant structure must be designed.

However, at very high fields where μw sources can often only provide milliwatts of power, or for samples containing lossy (μw attenuating) materials such as liquid water,[73] resonators may be the best choice to permit efficient EPR detection, as well as new and efficient methods to perform time-domain modulated DNP experiments such as TOP-DNP.[75]

An alternative approach is to use a non-resonant sample holder, which allow the use of a much larger sample volume (e.g. >10 μL at 200 GHz)[17,76,77] and the entire frequency bandwidth of the source, but at the cost of μw power. In this design, the μw field propagates through a sample holder (ideally) without standing waves or mode conversion. In the case of a corrugated waveguide, the μw beam is launched at the sample as a nearly gaussian beam. With a non-resonant EPR/DNP probehead, the goal is to guide the μw radiation to and from the sample with as little loss as possible, and without sacrificing NMR performance. Even for the design of a non-resonane sample holder, the geometry and materials of the sample holder are critical. Due to diffraction of the μw beam outside the waveguide,[78] the sample should be placed inside, or as close to the waveguide as possible, and reconcile this with an RF coil design that does not sacrifice RF performance. Alternatively, waveguide extensions can be used to guide the μw's to the sample positioned outside the waveguide.[17] Here, the sample diameter should not be much smaller than the waveguide aperture to maximize the μw filling factor. Furthermore, the sample geometry should be as thin as possible in the dimension parallel to the direction of the μw beam propagation– preferably no more than a quarter wavelength thick to avoid effects of B_1 in-homogeneity throughout the sample. However these considerations, again, restrict sample volume and can cause a reduction in NMR filling factor and B_1 field for typical NMR coil geometries.

For optimal μw transmission to the sample from the waveguide, the path of the μw should not contain high dielectric constant or conductive materials that could reflect μw's before they reach the sample. Similarly, materials with high loss tangents should not be placed near the μw path to reduce dielectric loss to heat. Materials such as PTFE (teflon), PFA, and Kel-F are excellent choices due to their suitability at cryogenic temperatures, low dielectric constant and loss tangents, and lack of protons (allowing ^{1}H NMR detection).[79] To further enhance the μw power at the sample, a mirror can be placed opposite at the bottom of the sample cup, causing the μw radiation to pass through the sample twice, theoretically doubling the μw power.[16,17,77]

3. Results: Design and Performance of Dual DNP/EPR Probe

The design of the Han lab probe described here made every effort to incorporate what we determined were the optimal design choices described in the previous section.

3.1. Thermal Design

3.1.1. Cryostat

The Han lab chose a close cycle cryostat to replace the previously used continuous flow cryostat for the dual DNP/EPR probe as the economically most sustainable solution. A new DNP/EPR probe was designed and built from scratch to fit into a close cycle cryostat custom designed by Janis (described below), replacing the continuous flow cryostat (Janis STVP-200-NMR) and DNP/EPR probe design used for DNP studies until 2019.[38,54,80–94] The Han lab close cycle cryostat consists of a Sumimoto CKW-21 helium compressor paired with a Janis custom SHI-500T-5 Gifford-McMahon (GM) cold head. The cryostat consists of a cold finger surrounded by a radiation shield, which is maintained in a vacuum jacket as shown in Fig. 1a-b. The copper cold finger located at the bottom of the cryostat is cooled by the cold head positioned below, which is powered by the helium compressor (Fig. 1c). The cold finger is in (conductive) thermal contact with the sample chamber, which is filled with helium gas and holds the sample cooled by gas conduction between the cooled inner bore and the sample. The cryostat is pressurized at 0.5 psi using an external helium tank, a pressure sensor, and a solenoid valve, electronically controlled by an Arduino microcontroller. This cryostat can reach an unloaded temperature of 4.2K (without a probe inserted).

3.1.2. Probe

Our dual DNP/EPR probe is built to minimize heat exchange between the ambient environment and the probehead containing the sample. To achieve that, the structural frame is constructed of a perforated thin cylinder of 316 stainless steel (316-SS), supported by disks made from soldered together FR-4 printed circuit boards (PCBs) that act as baffles to block gas conduction (Fig. 2a). The FR-4 PCBs are soldered to an aluminum PCB polished on one side to reduce thermal radiation. Polishing both sides could improve thermal performance and can be incorporated in the future. The waveguide (held within the aforementioned structural frame) is constructed of German silver, and the waveguide taper is made of gold plated copper to minimize interference with B_0 homogeneity around the sample from the German silver (which can be slightly magnetic due to its nickel content).[95] Notably, the waveguide presents a large, thermally conductive cross section that will facilitate unwanted heat transfer. As a waveguide material, stainless steel would be a poor choice due to residual magnetism resulting from the machining process even for non-magnetic variants, while titanium would be a poor choice due to the cost of the material and difficulties machining it. German silver has similar thermal expansion to stainless steel and similar thermal conductivity to titanium, without the downsides of each choice, while reasonably

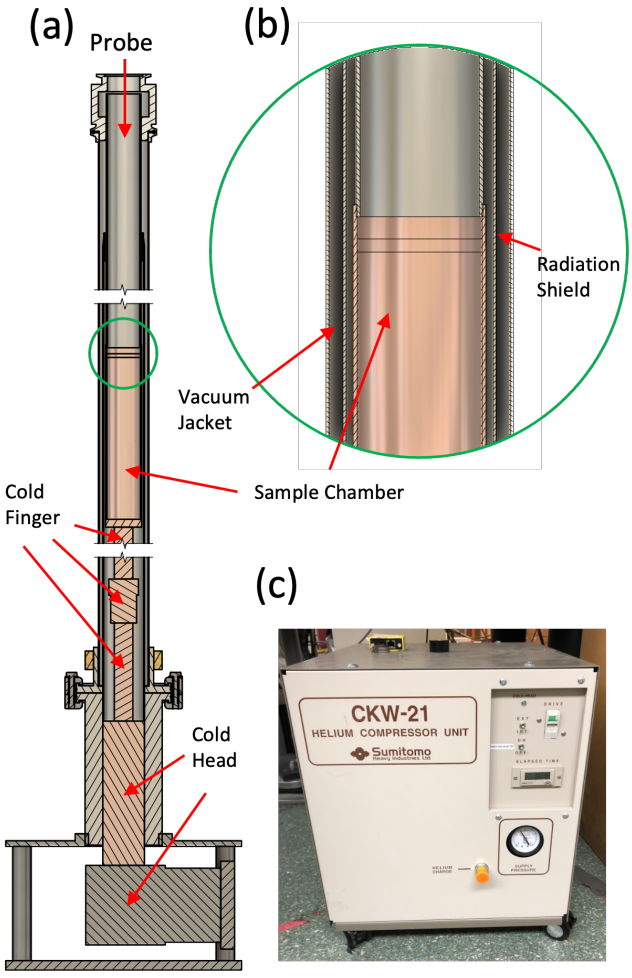

Figure 1: A) Cross section CAD model of the Janis Cryostat described in this paper. B) Zoomed in picture showing the concentric tubes used to form the radiation shield and vacuum jacket. C) Picture of the helium compressor used to power the cryocooler.

priced. A cross section of a probe baffle with all feedthroughs is shown in Fig. 2b.

The sample is held at the bottom of the waveguide by a "J arm" structure consisting of a 0.25" tube running the length of the probe, cross-connected to a sample mounting piece, as shown in a zoomed out photo, in Fig. 2c. The bottom 12" of the "J arm" nearest the sample cup is built from copper, while the upper part (~24") is built from 316-SS. The use of copper is to reduce any B_0 inhomogeneities that may be induced from the slightly magnetic 316-SS material near the sample, while the 316-SS reduces heat transfer along the thermally conductive copper to the sample.

The sample temperature is measured via a Lakeshore Cernox "SD" package negative temperature coefficient sensor mounted on the sample holder via an aluminum PCB (to facilitate thermal contact with the sample) as shown in Fig. 2c, and connected to a Lakeshore 350 temperature controller via wires fed through the J arm. Variable temperature is achieved by the addition of a 100 Ohm metal foil resistor to the PCB as a heater (Fig. 2c), which is fed current and controlled with a PID loop by a Lakeshore 350 temperature controller. The loaded, pre-cooled cryostat with the probe can reach a minimum sample temperature of 8.5 K after about 6 hours of cooling, as shown in Fig. 2d. Currently no sample exchange mechanism is in place and the entire probe must be taken out of the cryostat to switch samples. However, the crysotat can be left running while the probe is taken out to avoid fully warming the cryostat. Sample/probe exchange with a running cryostat can be achieved within 1 or 2 hours, depending on the exact operating temperature.

Additionally, a sweep coil is placed around the cryostat, inside the magnet, to enable field swept EPR and DNP experiments. Further information about the sweep coil is available in section 1.2 of the SI.

3.1.3. Improvements in Thermal Performance

The cryo-free cryostat can reach 4.2K without a probe, but only 8.5K at the sample with the probe inserted. This means modifications to the probe can allow achieving a lower sample temperature. The lowest temperature of the probe is mostly limited by the conduction of heat down the length of the corrugated waveguide. Hence, the thermal performance can be improved by adding a thermal break to the waveguide (i.e cutting a section of the waveguide out and leaving an air gap), which should have minimal implications to the μw performance.[96] This can help reduce the largest contribution to thermal conduction in the probe. Furthermore, the waveguide could be constructed from thermally less conductive material than German silver (e.g. stainless steel or titanium) and plated with gold to maintain surface conductivity. Finally, proper multi-layer insulation consisting of foam layers interspersed with reflective foil sheets can be implemented along the length of the probe to further block helium gas flow, and so reduce thermal radiation effects.

3.2. RF Design

The design aspects of the RF circuit and components were chosen to optimize the B_1 and detection sensitivity of both the

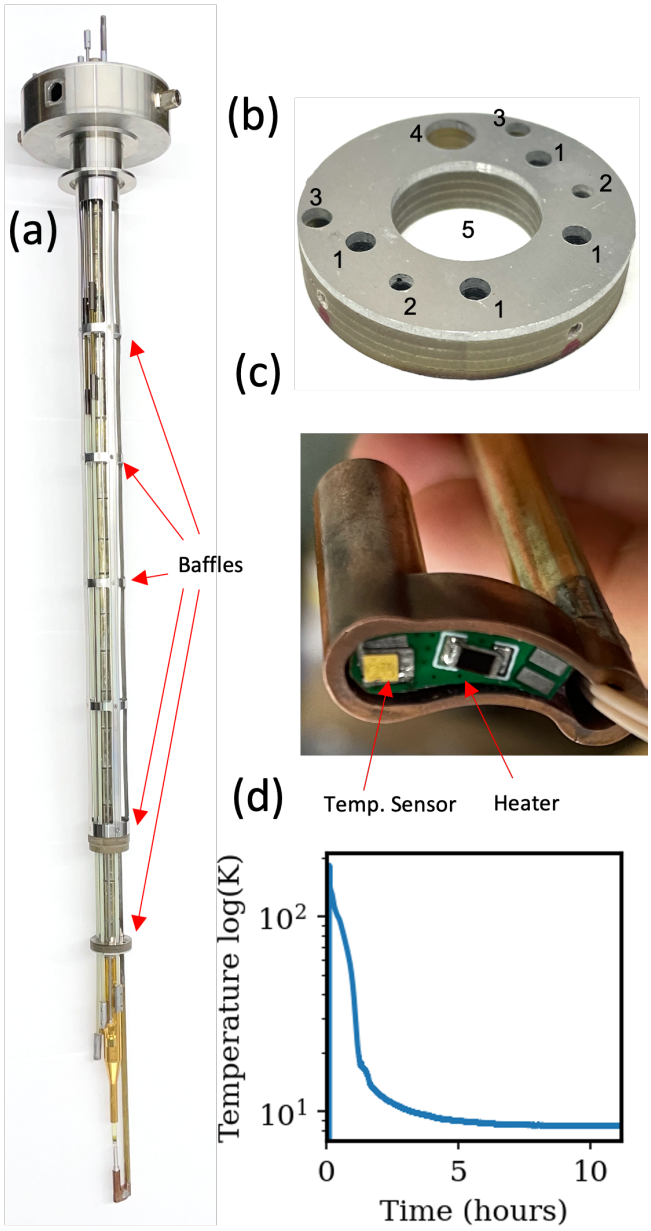

Figure 2: (a) Picture of probe without NMR circuit. The top of the probe is at room temperature while the bottom of the probe is at the lowest temperature. (b) Picture of FR-4/aluminum probe baffle with labeled feedthroughs: 1) G-10 tuning rods, 2) 0.085" 316-SS Coaxial cables, 3) 1/8" holes for future use, 4) J arm cutout, 5) waveguide.(c) J arm piece with PCB containing temperature sensor and heater. (d) Probe cooldown time when the cyrostat is already at the minimum temperature.

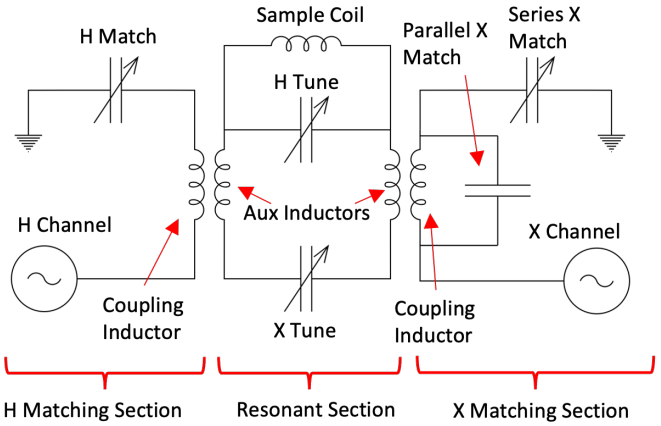

Figure 3: Layout of the inductively coupled double resonance circuit. The "inner" resonant portion of the circuit consists of the Sample Coil, the tuning capacitors "H Tune" and "X Tune", and the Auxiliary Inductors necessary to generate multiple resonances. The matching portion of the circuit consists of the matching capacitors "H match" and "X match" as well as the coupling inductors. The RF energy is fed into the matching portion of the circuit which transforms the 50 ohm impedance of the RF pulse to the impedance of the resonant portion of the circuit through the inductively coupled coils.

NMR and EPR spins.

3.2.1. RF Circuit Design

Our DNP probe design relies on a cryogenically tuned circuit by inductive matching. The basic principle of our cryogenically tuned, inductively coupled, rf circuit is schematically shown in Fig. 3. The design is based on the principle developed by Zens et. al[57]. Here, the "inner" resonant section of the circuit uses a doubly resonant 3 inductor "ladder" configuration, with the RF energy for each channel inductively coupled into the resonant portion through two equivalent auxiliary inductors as shown in Fig. 3. Matching is achieved by adjusting the series and parallel capacitance of the outer matching coupling inductors. This circuit provides all the advantages of a balanced, inductively coupled, circuit that also has a high inherent η_{CFF} due to the minimal number of discrete inductors used (the 2 auxiliary inductors shown are equivalent and only count as 1). Additionally, the design requirements (Q_T, power handling, etc.) of the matching sections (i.e coupling inductors and matching capacitors) can be relaxed as they are not part of the resonant circuit.

3.2.2. Capacitors

The fixed capacitors used in our probe are commercially available nonmagnetic Knowles Syfer 1111 package chip capacitors with a nominal DC voltage rating of 2kV (e.g. Digikey part number 1608-1268-1-ND). For the resonant portions of the circuit made up by tuning capacitance, 3 of these capacitors are used in series to increase the voltage handling (shown in Fig. 6a).

The variable capacitors used in our probe are mechanical capacitors, home-built from copper and zirconia to mitigate relatively frequent breaking and avoid the high cost of the commercially available variable capacitors, and to achieve the desired tuning and matching range. These capacitors work by ac-

tuating a copper piston (via a G10 tuning rod) in and out of the zirconia tube, which is itself wrapped in copper foil. The G10 rods are actuated via a simple screw mechanism located towards the top of the probe. The copper piston acts as one plate of the capacitor, while the copper foil cylinder acts as the other, with the cylindrical zirconia tube serving as the dielectric in between. The design for this variable capacitor illustrated in Fig. 4(a)-(c). A zirconia dielectric, which is a ceramic, was chosen to achieve good mechanical properties (i.e high fracture resistance) at low temperature, a high dielectric constant (allowing the capacitor to be smaller), a large dielectric strength (allowing larger P_{RMS}), and a fairly well matched coefficient of thermal expansion to copper (of which the foil and piston is made of) which prevents jamming of the capacitor.[97] Many capacitors use sapphire or alumina as the dielectric material due to their lower loss tangent, but in our experience the Q of the capacitor is larger compared to that of the inductors, such that it has a minimal effect on the overall Q of the circuit. Even using slightly more lossy zirconia as the dielectric has only a small effect (i.e > 10%), while zirconia is a much stronger material that is less prone to breaking.

One major issue we encountered with this capacitor design is arcing/partial discharge on the surface of the inner copper piston into the slight air gap that exists between the inner copper piston and the zirconia dielectric. Simulations show that for a simplified 3 plate capacitor design, the electric field density will always be greatest across a (low dielectric constant) air gap, as illustrated in Fig. 4 (d) and (e). This air gap always exists to some degree due to manufacturing tolerances that allow the inner piston to move vertically to adjust the capacitance. Since air has a much lower dielectric constant than zirconia, most of the electric field generated between the inner copper piston and outer copper foil is concentrated in the air gap, which also has a much lower breakdown voltage (especially when filled with helium). Furthermore the electric field in the air gap will always be strongest near the surface of the metal conductor. To solve this problem we used an 0.01" thick FEP heat shrink around the inner piston. This heat shrink creates a tighter fit around the inner piston. We demonstrated that this design adjustment largely eliminates the air gap on the surface of the piston. The highest electric field is thus concentrated in the FEP layer which has a much higher dielectric strength than air or helium. One drawback of this FEP layer is a smaller capacitance range, since the FEP layer is much thicker than any air gap that would otherwise exist, and it has a much lower dielectric constant than zirconia.

The overall construction of the tuning capacitor is shown in Fig 4a-c. Fig 4b-c shows the X channel capacitor that has a maximum capacitance range of 1-6pF, can handle ~1000 volts peak to peak at 300 MHz without arcing (in ambient atmosphere at room temperature), and has a $Q >> 300$ (measurement methods shown in sections 2.2 and 2.3 of the SI). The observed breakdown occurs across the gap between the two outer pieces of copper foil, and thus the capacitance range can be traded for increased power handling by making the outer copper foil pieces shorter and further apart. This was done for the H channel capacitor (as shown in section 2.4 of the SI) where the capacitor plates are also horizontally arranged to provide shorter

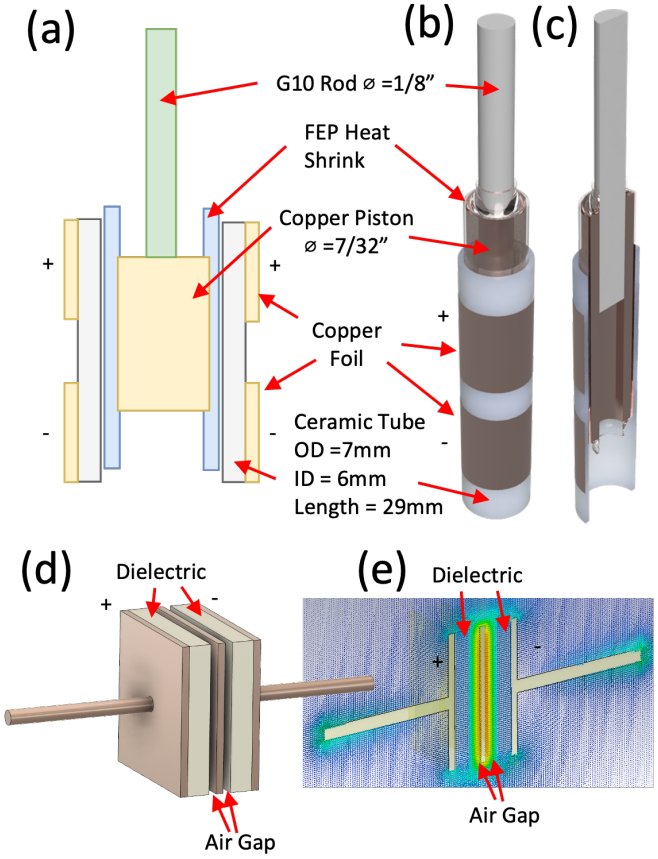

Figure 4: (a) Schematic of the capacitor construction. (b) Rendering of the X channel tuning capacitors used. (c) Cross section of the X channel tuning capacitor. (d) Simplified 3 plate capacitor with high dielectric constant ceramic material (i.e zirconia) between the plates, and an air gap around the central plate. The two ends of the capacitor connected to an outside circuit are indicated by + and -. (e) Simulation result showing the relative electric field density on a cutout of the simplified 3 plate capacitor. The electric field of the capacitor is concentrated in the air gap.

lead lengths to the sample coil, and so yield a ~1100 Vpp power handling on the X channel at higher frequency.

The matching capacitors are similarly constructed using a zirconia tube, copper piston and copper foil, however no FEP heat shrink was used and one end of the capacitor is directly grounded (as shown in section 2.5 of the SI). This is because the matching capacitors do not need to handle high voltages unlike the tuning capacitors, as they are not part of the resonant circuit; but, a larger capacitance range still can extend the tuning/matching range of the circuit.

These homebuilt variable capacitors are much cheaper than commercial capacitors (the major cost is the Zirconia dielectric tubes), are mechanically much more robust to resist repeated thermal cycling between liquid helium and room temperature, and are customized to suit our specific needs in terms cryogenic operation, RF tuning range and RF voltage handling.

3.2.3. Inductors

We chose a 4 turn saddle coil for NMR signal detection to allow for axial μw irradiation and to achieve a (relatively) high

inductance (compared to an alderman grant coil) necessary to double tune our RF circuit to the correct frequencies (~300 MHz and 74 MHz for the H and C channel, respectively), and to ensure high RF efficiency. The coil is constructed from vertical copper rods (1mm/18 AWG wire) connected by horizontal copper wire to form the saddle coil as shown in Fig. 5a-c. The coil diameter is 9.5mm, the window angle is 110° (although any angle over 90° is sufficient)[98], and the window height is 7mm. The vertical wires are supported by holes machined into 2 PTFE rings (Fig. 5a) which are mounted around a 7mm OD zirconia support tube. Copper foil guard rings (shown in the cutout of Fig. 5c) are placed inside the zirconia tube to focus the RF field onto the sample, as well as prevent excess μw scattering, as will be discussed later.

The coil parameters were measured by resonating the coil at the desired frequency (300 MHz for H and 74 MHz for X nuclei) using a chip capacitor across the coil leads (not within the RF circuit) and coupling the coil to a VNA (vector network analyzer) using a pickup loop. The coil was found to have an inductance of 125nH, and a measured Q_T of 205 at 74 MHz and 275 at 300 MHz, respectively (as shown in Fig. 5d). The z axis homogeneity of the coil was determined from ball shift measurements (see section 2.6 of the SI) using a 1/8" aluminum ball.[99] The ball shift profile is shown in Fig. 5e, showing that the homogeneous B_1 region of the coil spans about a 3mm height, as shaded in red. This measurement suggests that a fairly good RF homogeneity (less than 10% variation in amplitude along the z axis) for the H and X channel in the sample, as long as the sample height is not taller than 3 mm.

For the circuit described in this paper, the auxiliary coils are two-turn solenoid coils with an ID of 7mm wound from 14 AWG wire (shown in Fig. 6c below). These coils have an inductance of 51.5 nH when the lead lengths are included, and a Q_T of 410. The coupling inductors used to couple to the auxiliary coils are two- and three-turn (for H and X channel respectively) 7mm ID solenoid coils wound from 18 AWG copper wire. These coils are aligned axially with the auxiliary coils to achieve the desired magnetic coupling. The exact inductance, Q, and the coupling factor k (i.e the overlap of magnetic flux from the matching and auxiliary inductors) does not necessarily need to be tightly controlled as they minimally affect the circuit performance. A higher k and larger inductance will generally make the circuit easier to match (especially at lower frequencies), but caution must be taken not to increase k too much, as this will be deleterious to the RF efficiency and Q. If optimal matching can be achieved (>25 dB return loss) a lower k and inductance value can be used that will slightly increase the circuit performance (as less magnetic energy will be stored in the coupling inductors). For lower frequencies and lower coupling factors, the coupling inductors can be made resonant near the desired tuning frequency (i.e 74 MHz for the X channel) by placing a capacitor across the coupling inductor (as shown in Fig. 3) to facilitate matching.[57]

3.2.4. RF Circuit Construction

The RF circuit constructed from the capacitors and inductors are shown in Fig. 6. The exact circuit diagram with each discrete component used and their value is shown in Fig. 6a (for a circuit dually tuned to ^{1}H and ^{13}C). The circuit components are supported by grounded aluminum plates and standoffs as shown in Fig. 6b, and can be divided into two parts which are separated by the aluminum plates. The upper "deck" contains the matching circuitry, coaxial cable feeds, and auxiliary coils; and the lower deck contains the sample coil and tuning capacitors. Most of the coaxial cable consists of a 0.085" 316-SS coaxial cable with a silver plated beryllium copper center conductor, but the bottom 5" length feeding the RF circuit is made of a 0.141" copper coaxial cable to minimize disturbance to the B_0 homogeneity by the slightly magnetic 316-SS material. All leads that connect the discrete RF circuit components are made of 14 AWG copper wire with occasional application of FEP heat shrink to prevent shorting components together or to ground, and are soldered with a 60/40 tin-lead solder. The distance between the coupling inductors and tuning inductors is about 4mm, but can be adjusted by hand to get k between the coupling inductors and the auxiliary inductors into the correct range to match the circuit. Most of the capacitance for the H channel is placed directly across the coil leads in the form of three 12 pF chip capacitors in series, as shown in Fig. 6a. This improves η_{CFF}, as most of the H channel current travels directly through the chip capacitors and not through the leads to the variable capacitor, which have inductance and can reduce the overall circuit efficiency, η_{CFF}. The X channel tuning capacitor is brought into the correct range by the addition of three 33 pF capacitors in series (Fig. 6a). For both the H and X channel the chip capacitors are placed in series to extend their voltage handling to be equal or better than the variable capacitor. Pictures of the constructed circuit are shown in Fig. 6b-c. Here the saddle coil, home-built capacitors, and auxiliary coils are visible.

The performance of this circuit is shown in table 1. The Q_T for the circuit is 281 and 170 for the H and X channels respectively. These are not very impressive numbers in comparison to a commercial solid-state NMR probe, but the lower Q values can be mostly attributed to the small size and construction of the sample-holding saddle coil (which itself has a similar Q as shown in Fig. 5d). The max power handling of the circuit is 150 W for the H Channel and 125 W for the X Channel, which is mostly determined by the power handling of the variable capacitors. The η_{CFF} was measured experimentally using ball shifts (described in section 2.6 of the SI), which yielded a H channel η_{CFF} of 32.9% and an X channel η_{CFF} of 63.3%. The η_{CFF} balance between these channels was deliberately optimized through the design of the auxiliary coils to maximize the X channel detection sensitivity after cross-polarization (CP). The total observed η_{CFF} of 96% is high, which is achieved owing to minimal parasitic and unnecessary inductance in the circuit design. At 125 W input power, the B_1 was measured to be 50 kHz (corresponding to a 5 μs 90° pulse) for the H channel and 31.25 kHz (corresponding to a 8 μs 90° pulse) for the X channel, respectively at room temperature. Additionally, the tuning range of the X channel in the shown configuration is 69-81 MHz, which gives access to ^{55}Mn, ^{79}Br, ^{13}C, ^{27}Al, ^{51}V, ^{23}Na and ^{63}Cu nuclei. This performance is low compared to most

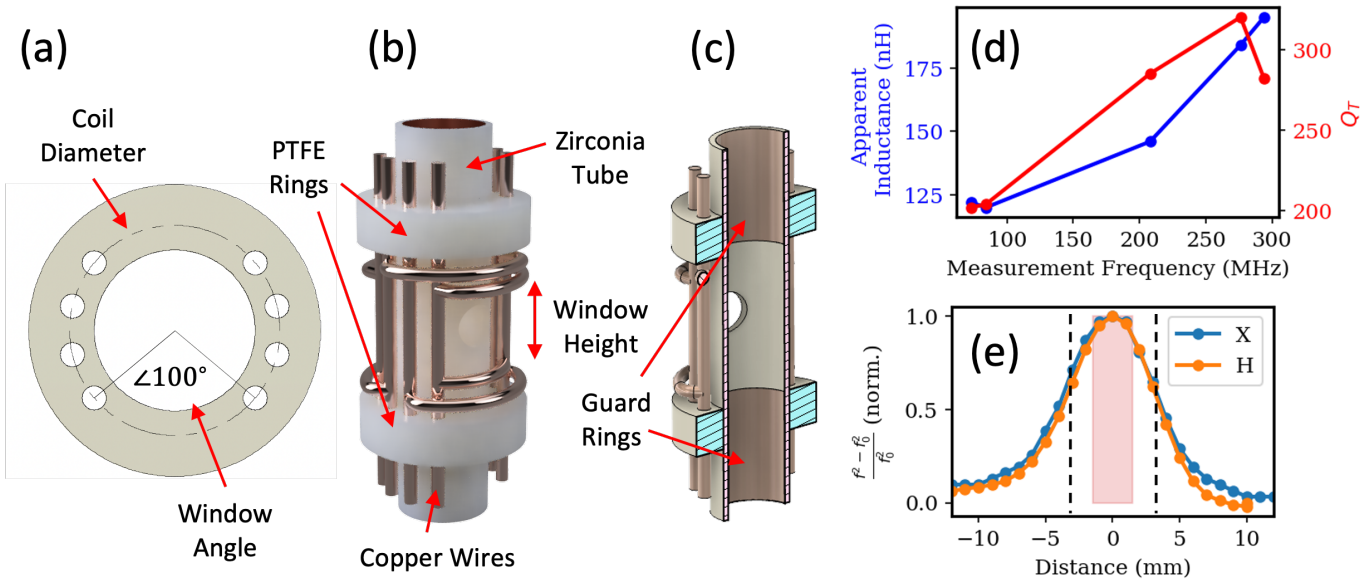

Figure 5: (a) Top down schematic of the PTFE Support rings used to form the saddle coil. (b) Rendering of the 4 turn saddle coil with PTFE rings, zirconia support tube, and copper foil guards. The coil is formed by inserting vertical copper wires into the holes in the PTFE rings and cross connecting them by soldering horizontal lengths of copper wire. (c) Cutout of coil showing copper foil guard rings. (d) Coil inductance and Q_T at different frequencies. (e) Ball shift measurement at 74 MHz (X) and 300 MHz (H). The window height is indicated by the black dashed lines, and sample region is shaded in red.

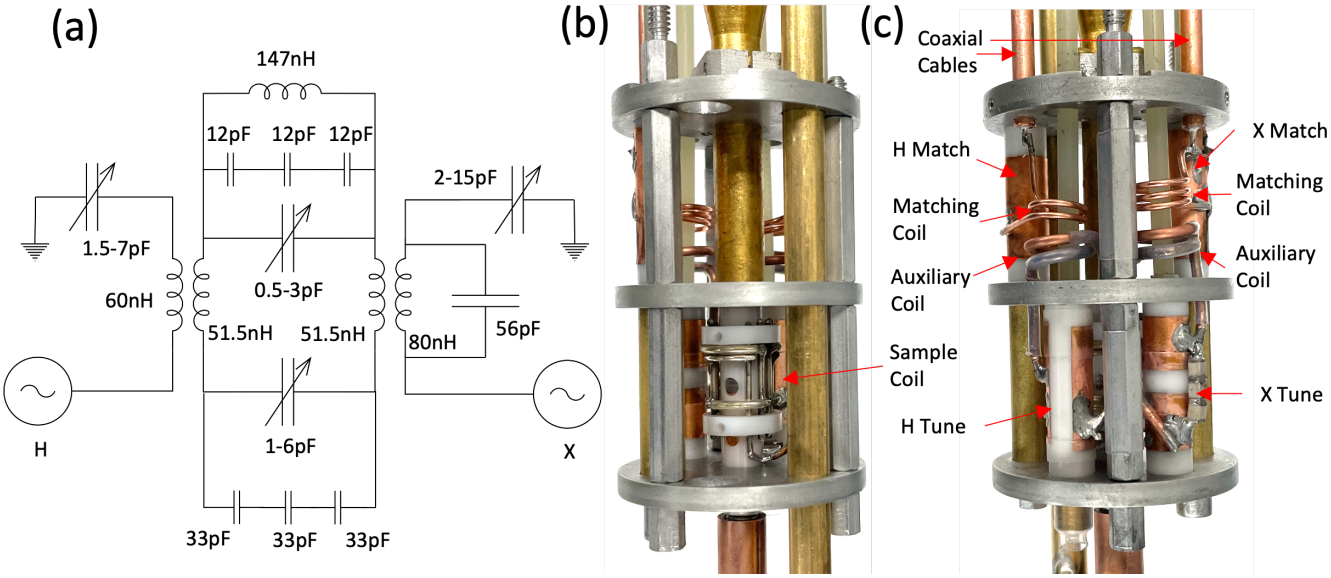

Figure 6: (a) Schematic of inductively coupled (H-X) double resonance circuit with all discrete component values shown. (b) Picture of the constructed circuit attached to the waveguide taper with components indicated.

Channel	Q_T	Max Power	η_{CFF}	B_1 (125 W)
^{1}H	281	150 W	32.9%	50 kHz
^{13}C	170	125 W	63.3%	31.25 kHz

Table 1: Performance and parameters of the inductively coupled double resonance NMR circuit.

solid-state NMR probes using solenoid coils (as is the case for most MAS systems), but is excellent for saddle coil-based systems, especially considering the large diameter of the saddle coil.

3.2.5. Improvements to RF Design

While the RF circuit performs well, and care has been taken to optimize most aspects of the circuit, there is room for improvement, mainly through modifications of the sample coil. If the coil could be wound from a single wire (instead being soldered together), the Q and η_s would be higher. Additionally a flat coil made from foil could increase the η_s over that wound by round wire used here. Guard rings outside the coil could be placed to focus the B_1 field more into the sample and further increase the η_s. The variable capacitor geometry could also be changed to provide a shorter path for the RF current, hence increase η_{CFF} by reducing parasitic inductance.

3.3. μw Design

3.3.1. μw Transmission

The μw transmission starts with a gaussian beam from a source that is guided through a quasi-optical table, then bent downwards and fed into a corrugated waveguide that is built into the probe placed within a vertical 7 Tesla magnet, as described in a previous paper.[17] The top of the waveguide is vacuum sealed with an epoxy sealed rexolite window. The μw transmission down the probe is achieved via a 12.7mm ID corrugated waveguide (Bridge12 Inc) constructed from nickel silver (i.e German silver). The end of this corrugated waveguide is connected to a gold plated waveguide taper whose ID transitions from 12.7 mm to 5.5mm ID to focus the μw's onto the sample, as shown in Fig. 7(a-d).

3.3.2. Sample Cup Construction

The sample holder for our dual EPR/DNP probe is constructed of a 3/16" OD, 1/8" ID PFA tube with 1/8" PTFE rod inserts to hold the sample in place, as well as an aluminum insert that acts as a mirror, as shown in Fig. 7(c)-(d). The bottom of the PFA tube is threaded to enable mounting the sample to the "J arm". The sample volume can be altered by adjusting the length of the PTFE inserts/plugs such that the sample is situated within the homogeneous region of the NMR coil, which allows a maximum sample volume of ~30μL. The advantage of this design is that all parts are readily and cheaply commercially available, and the sample holder is easily assembled, so that re-use of sample cups is not necessary. Samples can be simply saved in the sample cup for later use, if needed.

3.3.3. Sample Cup Optimization

Although the sample cup is made from commercially available parts, the geometry was carefully designed to ensure maximum transfer of μw power to the sample. The PFA/PTFE sample cup itself acts as a dielectric waveguide, which was inspired by the work of Zilm et. al (Private communication, Kurt Zilm, Anne Carroll). Here, the μw's are confined in the PTFE structure due to the higher dielectric constant of PTFE compared to free space. Additionally, PTFE/PFA has a low enough dielectric constant to not cause too much reflection off the surface of the sample cup. The geometry of this PFA/PTFE waveguide was optimized using finite difference time domain (FDTD) techniques using the CST Studio software. Selected geometric features that were optimized, in feedback with FDTD simulations, are shown in Fig. 8a, as well as the SI Fig. S7.

In these simulations the μw power was measured as a function of the various geometric features, with a typical simulation result/setup shown in Fig. 8b. Here, a cross section of the RMS B_1 field amplitude in the sample cup/waveguide extension is shown for a frequency of 194 GHz. The simulation model shown here includes the corrugated waveguide, PFA/PTFE waveguide extension, sample, and support tube. The μw output of the corrugated waveguide was simulated using a TE_{11} to HE_{11} mode converter structure with the same output ID as the actual waveguide.[100] For simplicity, the waveguide was simulated as a perfect electrical conductor. The PFA/PTFE waveguide extension/sample cup was modeled as a solid PTFE rod (dielectric constant $\epsilon = 2.1$), and the sample was simulated as a puck of frozen DNP Juice ($\epsilon = 3.5$).[101] This model does not include the aluminum mirror as this feature greatly increases the simulation time and makes interpretation of the results more complicated.

It is qualitatively apparent that most of the μw power is confined to within the PFA/PTFE waveguide extension volume, and is not radiating away from the sample. Thus, most of the μw power will intersect the sample and yield higher B_1, which is useful for EPR and DNP performance.

The final sample cup geometry used in our probe was optimized using calculations of the percent B_1 field to sample (shown in Fig. 8c-f), with the select geometrical dimension indicated by the dashed lines. Fig. 8c shows the results of the waveguide taper extension diameter (labeled as "diameter of sample cup" in Fig. 8a) on the effective "filling factor". Here, the filling factor is measured as the % of μw power that passes through the upper face of the sample (more information is available in section 3.1 of the SI). Fig. 8c shows that for larger diameters, the % of μw power that gets to the sample decrease from almost 80% for a 3mm diameter to ~30% for a 10mm diameter taper. This effect can be qualitatively seen in the SI Fig. S10. Taken all together, we chose a 3/16" (4.76mm) waveguide extension diameter (dashed line on Fig. 8c) to achieve an optimal filling factor while maintaining a reasonable sample diameter/volume. Additionally, confining the μws to a smaller volume makes the sample thinner, allowing a thinner NMR coil, which can give a higher NMR B_1.

Fig. 8d shows the effect of the gap between the waveguide

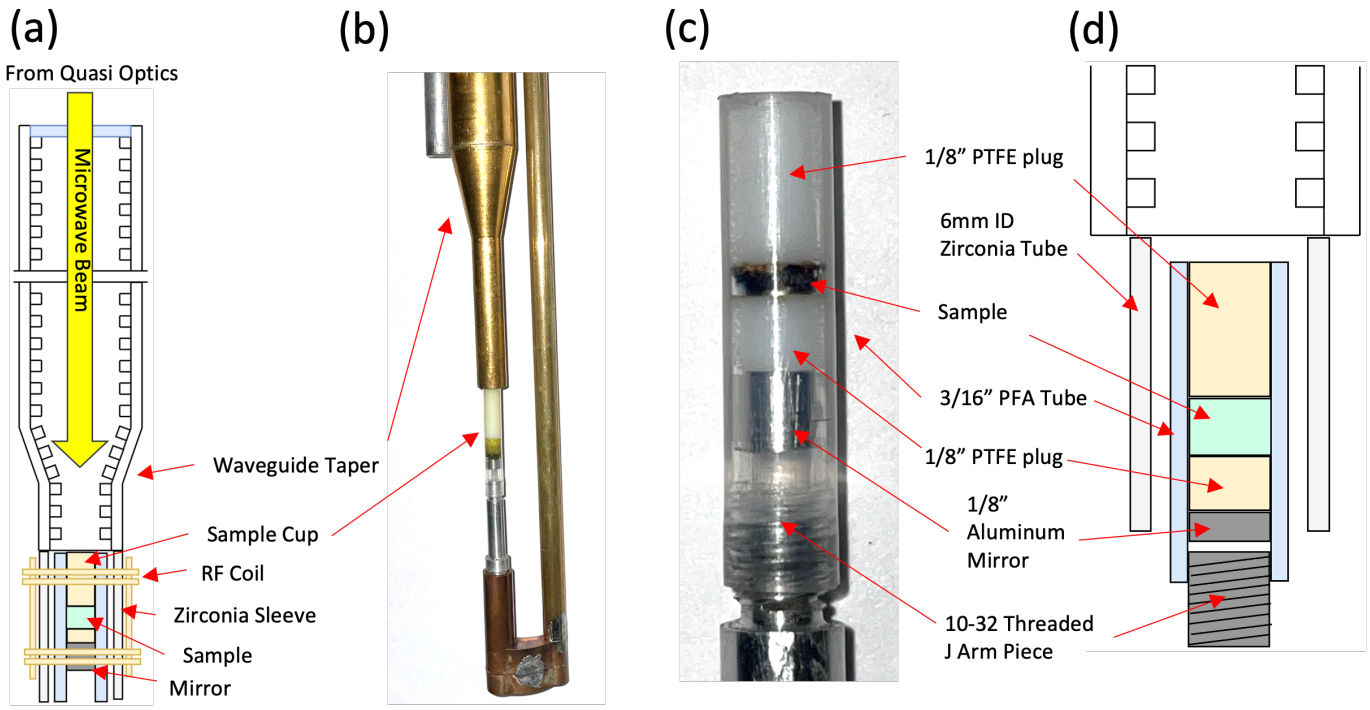

Figure 7: (a) μw pathway to sample. (b) Picture of waveguide taper, sample cup, and J arm without RF circuit. (c) Picture of sample cup. (d) Schematic of sample cup.

extension and the RF coil support tube. This parameter affects the diameter of the sample cup and/or the inner diameter of the coil support sleeve. The gap can be seen as the white space between the grey coil support sleeve and the blue sample cup labeled as "gap between sample cup and coil support sleeve" in Fig. 8a (and in the SI Fig. S7). From the simulation results we can see that larger gaps will yield higher μw filling factors, with a 0mm gap (no gap) giving ~28% filling factor and a 2mm gap giving ~80% filling factor. If this gap is too small the μws in the waveguide extension will couple to the tube and be scattered away from the sample. This concept is illustrated in the SI Fig. S11. However if the gap is too large, then the NMR filling factor will decrease as the NMR coil will have a larger diameter than necessary (either the sample cup is thinner or the RF coil is larger in diameter). Noteably, the gap has to exceed a threshhold value optimal for filling factor. The dashed line indicates the gap chosen for our probe geometry, which is ~1.2mm.

Fig. 8e shows how the waveguide extension length affects μw power to the sample. This determines how long the waveguide extension can be before μw's scatter out of the PFA/PTFE structure. It is important that the waveguide extension is long enough so that the metallic corrugated waveguide taper does not interfere with the NMR coil, but short enough that most of the μw power reaches the sample. The results suggest that the waveguide extension is very efficient at transmitting μw power, even at longer distances exceeding 10 mm. For our probe we chose length of ~9.5mm, which separates the NMR coil sufficiently from the corrugated waveguide, while not sacrificing any μw filling factor.

Last, but not least, Fig. 8f shows the dependence of μw filling factor on the position of PTFE waveguide extension relative to the waveguide (i.e the "sample cup distance from waveguide" as shown in Fig. 8a, and SI Fig. S7). Here a negative distance corresponds to the PTFE waveguide extension being placed partially inside the corrugated waveguide, and a positive distance corresponds to a gap between the output of the corrugated waveguide and the PTFE waveguide extension. The simulations show that in general, a larger gap results in less μw coupling between the corrugated waveguide and PTFE waveguide extension. However, the results also suggest that placing the PTFE extension inside the waveguide does not necessarily provide better coupling, but also does not diminish the coupling by much. These results are further illustrated in the SI Fig. S13. Thus we decided to position the PTFE extension directly at the output (0mm distance) of the corrugated waveguide for most situations.

4. Results: Dual DNP/EPR Experiments

4.0.1. μw performance of the DNP/EPR probe

To test the EPR performance of the sample holder, the EPR nutation frequency was measured. This is a good measure of performance because equations (1) and (2) hold for EPR and NMR signal, where higher μw B_1 translates to higher s/n. The nutation experiment was performed using a solid echo pulse sequence where the echo pulses are varied in length (as shown in Fig. 9a). Here, using a 90° pulse length should result in the highest detected EPR signal.

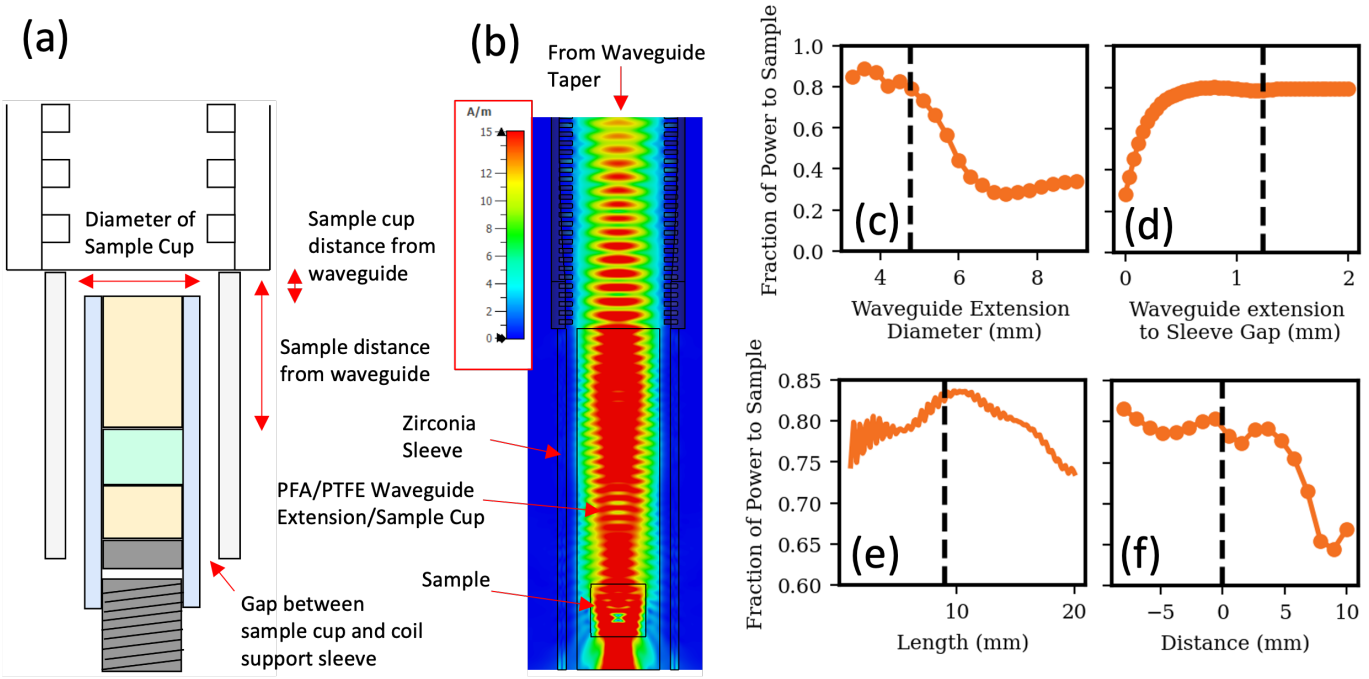

Figure 8: (a) Schematic of sample cup/waveguide extension simulation. (b) Cross section of the RMS μw B_1 field in the sample cup. (c) Average μw B_1 field and filling factor (i.e the percent of μw power that passes through the sample) as a function of the waveguide extension/sample cup diameter. (d) μw filling factor as a function of the gap between the waveguide extension and NMR coil support tube. (e) μw filling factor as a function of how long the waveguide extension is. (f) μw filling factor as a function of sample cup distance from waveguide. Negative numbers correspond to the top of the PTFE waveguide extension being inserted into the corrugated waveguide. For (c-f) the chosen geometry used in our probe is indicated with a dashed black line. Additionally each parametric simulation was carried out with all other geometric features held constant at the values indicated.

With the current optimization, our dual DNP/EPR probe yields a μw B_1 of approximately 500 kHz (corresponding to a 90° pulse length of 500 ns), as measured with 0.5% BDPA in polystyrene (data shown in Fig. 9a-b) using a 450 mW μw source. This B_1 for EPR detection is comparable to values reported previously from our lab.[17] Notably this value is just an average– because the sample dimensions (3mm for this sample) are larger than a quarter of the μw wavelength ($\sim$ 0.385mm at 194 GHz) there will be large variations in B_1 field across the diameter of the sample (uneven μw power distribution across the sample can be seen in Fig. 8b). Typically, the detection sensitivity for EPR in a typical configuration allows us to readily measure radical concentrations at or above 0.1 mM, depending on the EPR linewidth and relaxation time.

To verify the validity of the simulated μw performance, the B_1 for different configurations of the sample cup/waveguide extension was measured, as shown in Fig. 9d-h. The optimal configuration for EPR is to place the sample cup inside the waveguide, as illustrated in Fig. 9d. This ensures that minimal μw power is lost to scattering and yields a 90° pulse time of 700 ns with a 120 mW μw source. However, for dual NMR/EPR detection, the sample cannot be placed inside the solid metal waveguide because this prevents NMR detection. Fig. 9e shows a geometry closest to that used in our probe (shown in Fig. 7) including a length of 9mm and a 0.8mm gap between the outer tube and waveguide extension, which gives a 90° pulse of 1000 ns. The effect of lengthening the waveguide extension to 15mm is illustrated in Fig. 9f. This geometry yields an only slightly longer 90° pulse of 1050 ns compared to that in Fig. 9e, suggesting that the waveguide extension can be fairly long without losing too much μw power. This concept was demonstrated in the simulated results shown in Fig. 8e. Fig. 9g illustrates a scenario where the gap between the waveguide extension and coil support tube is eliminated, or equivalently, where the waveguide extension has a larger diameter (3/8" in this case) than the sample diameter. Here, the 90° pulse length doubles to 2000 ns (i.e a much lower B_1), which indicates that the predictions arising from the simulated results shown in Figs. 9c and 9d are correct, and that smaller waveguide diameters help focus the μw power to the sample. Fig. 9h shows a configuration in which the top of the waveguide extension is inserted 6mm into the corrugated waveguide. Here we notice a slight increase in the B_1 field (950 ns 90° pulse). This suggests that the μw couples into the waveguide more effectively, supporting the simulated predictions in Fig. 8f.

4.0.2. Improvements to μw Design

While substantial efforts have been made to optimize this DNP probe for EPR detection, there are still more improvements that can be made. PTFE is a good material for μw transmission, but it still cause reflections due to its relatively high dielectric constant compared to free space (2.1 vs 1). Thus with the current waveguide extension, some μw will always be reflected off the interface between PTFE and air. This can poten-

tially be reduced by adding specific geometric features to this interface, such as using a hemispheric lens or adding an anti-reflective coating to the PTFE probe elements. Furthermore, the sample diameter can be increased, allowing the use of thinner sample volumes (and higher μw B_1). The position of the mirror behind the sample also plays a role in the B_1 amplitude experienced by the sample, where careful simulations could reveal a more optimal position or mirror geometry (i.e a concave instead of flat mirror). For some DNP and EPR experiments, broadband μw performance is less important than achieving a high B_1 amplitude. In this case it may be beneficial to design a FP resonator between the waveguide and the mirror, and to tune the structure via precise actuation of the J arm, resulting in a resonant structure that can provide a higher μw field to the sample at the expense of μw bandwidth.

4.0.3. RF performance of the DNP/EPR probe

The performance of the dual DNP/EPR probe for dual NMR and EPR detection was evaluated and summarized in Fig. 10. The EPR/NMR pulse sequences used for each measurement are shown in the inset of each figure panel. The measurements were performed on a sample consisting of 20μL 40mM 4-Amino Tempo and 1M ^{13}C enriched Glycine in "DNP Juice" (i.e 60/30/10 d-Glycerol/D_2O/H_2O) at 23K, and include an echo-detected EPR field profile (Fig. 10a), an echo-detected EPR frequency profile (Fig. 10b), an echo-detected pump-probe ELDOR profile (Fig. 10c), and a ^{1}H$-^{13}$C Cross Polarization (CP) DNP profile (Fig. 10d), plotted on the same μw frequency axis for all plots (the field axis on Fig. 10a is scaled to be equivalent to the frequency axis). This allows us to compare the effect of electron spin density (field/frequency sweep) and spin diffusion (ELDOR) on the shape of the DNP frequency profile. We observe that the DNP frequency profile has a dispersive shape, which spans the EPR profile, indicating a cross effect mechanism. These broadband μw measurements are possible because of the non-resonant sample holder design of this dual DNP/EPR probe. This feature is critical in permitting EPR frequency dependent measurements spanning a frequency tuning range of 1 to 10 GHz. The ability to perform frequency stepping is advantageous over field stepping because they can span a greater range of EPR resonance compared to a room temperature field coil (in our setup, our sweep coil can reach +/-17mT or equivalently ~1 GHz), and because such measurements can be performed much faster than field swept measurements (jumping of μw source frequency is much quicker than changing field). Most importantly, the ability to generate and detect at multiple μw frequencies simultaneously or in rapid (μs to ms) succession is necessary to perform for two frequency (EPR) pump-probe experiments, such as ELDOR. Furthermore, μw frequency sweeping allows for the measurement of a DNP profile without retuning the NMR probe for each field position. However, our results also show that the shape of the frequency sweep (Fig. 10b) is slightly distorted compared to the field sweep (Fig. 10) due to interference from standing waves present in the probe and the quasi-optical μw bridge. The standing waves mostly affect the shape of the EPR frequency profiles or any experiment where the μw/EPR probe frequency is changing, while the shape of the ELDOR and DNP profiles are less affected as there, the μw/EPR pump frequency is stepped, but not the μw/EPR probe frequency.

Standing waves can be reduced by careful alignment of the bridge/probe (especially ensuring that the microwave beam is focused onto the waveguide of the probe and is not clipped), but this issue will always be present in some capacity. Thus, it is advantageous to be equipped with a field sweep coil, in addition to having access to μw frequency tuning.

Next, measurements were performed of the same sample as discussed at 23 K and 8.5 T, but this time using a narrow-line radical sample consisting of 20μL of 40mM OXO-63 trityl in DNP juice. A high concentration of trityl radicals have been shown to be a promising class of DNP polarizing agents at high field, while their underlying DNP mechanism is still subject of current interest.[88?] Using our dual DNP/EPR probe, we measured an EPR field and frequency profile (Fig. 10e) that reveals a distorted/split line-shape. This line-shape is most likely due to clustering of the radicals, leading to a distribution of electron-electron dipolar couplings.[?] In Fig. 10f the saturation recovery of the trityl EPR resonance is measured at various frequencies of the EPR spectrum (marked by dashed lines on Fig. 10e). The saturation recovery curves clearly illustrate that there are different components present in the EPR line that possess different T_1 relaxation properties. For example, the saturation recovery profile at 193.66 GHz (i.e in the "dip" region of the EPR profile) shows a much longer and distorted buildup curve, indicating the presence of multiple relaxation components with multiple T_{1e} rates.

Further interpretation of these EPR properties of this radical and their effect on DNP enhancements and properties require additional experiments. However, even the simple EPR field and frequency profiles, together with the EPR frequency/field dependent relaxation measurements is characteristic of an inhomogeneously broadened EPR line made up of heterogeneous electron spin populations with distinct frequencies. Such insight cannot be deduced from NMR-detected DNP experiments or simulations. Hence, concurrent measurements of EPR and DNP properties are key to the study of DNP mechanisms. Additional experiments that can be readily carried out (not shown here) include EPR T_m measurements, DNP buildup time profile and DNP power profile measurements.

5. Conclusion

In this paper we have described the design principles and construction of a dual EPR/DNP probe operating in a cryo-free cryostat operating down to 8.5 K temperatures. This system was constructed to simultaneously optimize stable operation at cryogenic temperatures, and to achieve robust EPR and NMR performance with as few compromises as possible. This was achieved through careful design choices of NMR RF circuit components and simulation of μw/EPR structures. This probe was constructed with a focus on multi-frequency/broadband EPR and NMR performance to enable a wide variety of experiments on samples with a broad range of EPR and NMR properties, as demonstrated via select EPR and DNP results on typical

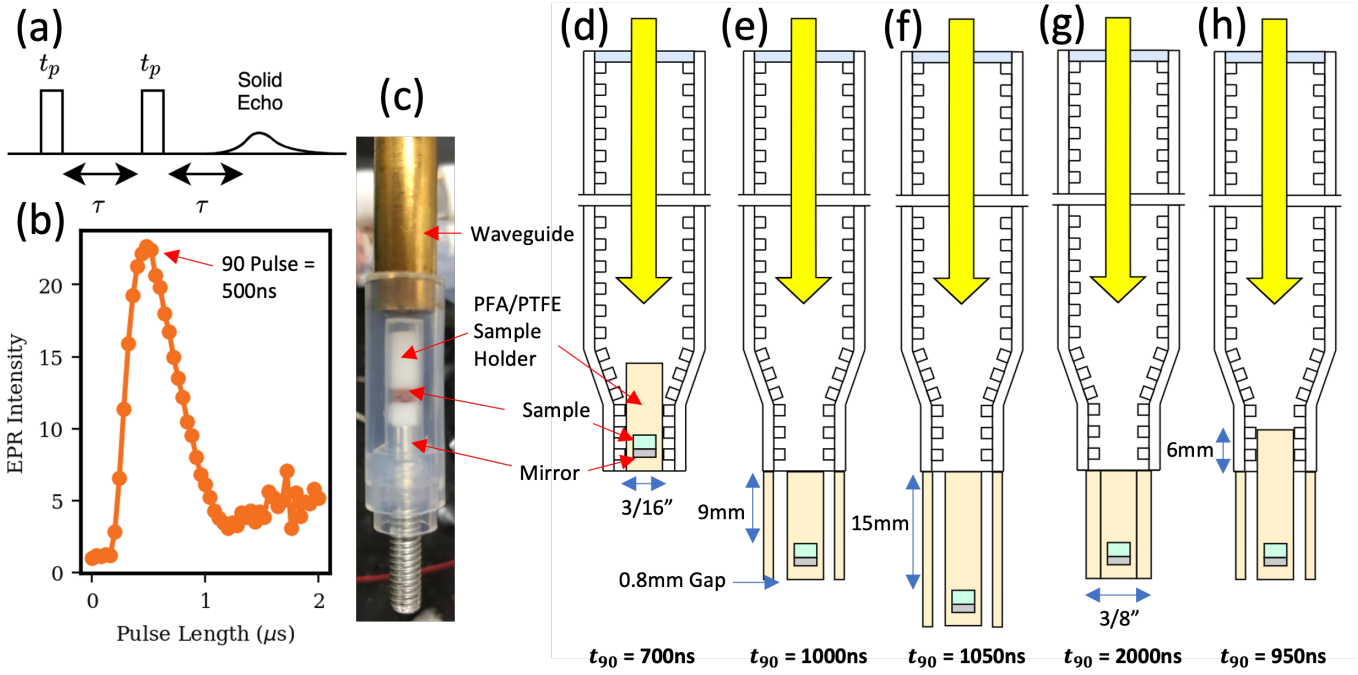

Figure 9: (a) Solid echo pulse sequence used for nutation experiment. (b) Nutation curve for a 0.5% BDPA in polystyrene sample using a 450mW solid state source. (c) Photo of the setup used to measure B_1 as a function of sample geometry in (d-h). Concentric PFA tubes were used to hold the waveguide extension in place. This is slightly different from the setup shown in Fig. 7 because the outer tube is PFA instead of Zirconia and has a larger OD, but should work to show proof of principle for simulations in Fig. 8. (d) The optimal arrangement for EPR detection and B_1 with the sample completely inside the waveguide. (e) Standard sample geometry arrangement with relevant dimensions labeled. (f) Geometry with a longer waveguide extension. (g) Geometry with no gap between the waveguide extension and a PFA sleeve– equivalent to a waveguide extension with a larger diameter. (h) Standard sample geometry with the waveguide extension inserted partially into the waveguide. For (d-h) the B_1 was measured with a 120mW source instead of the 450mW source used in (b).

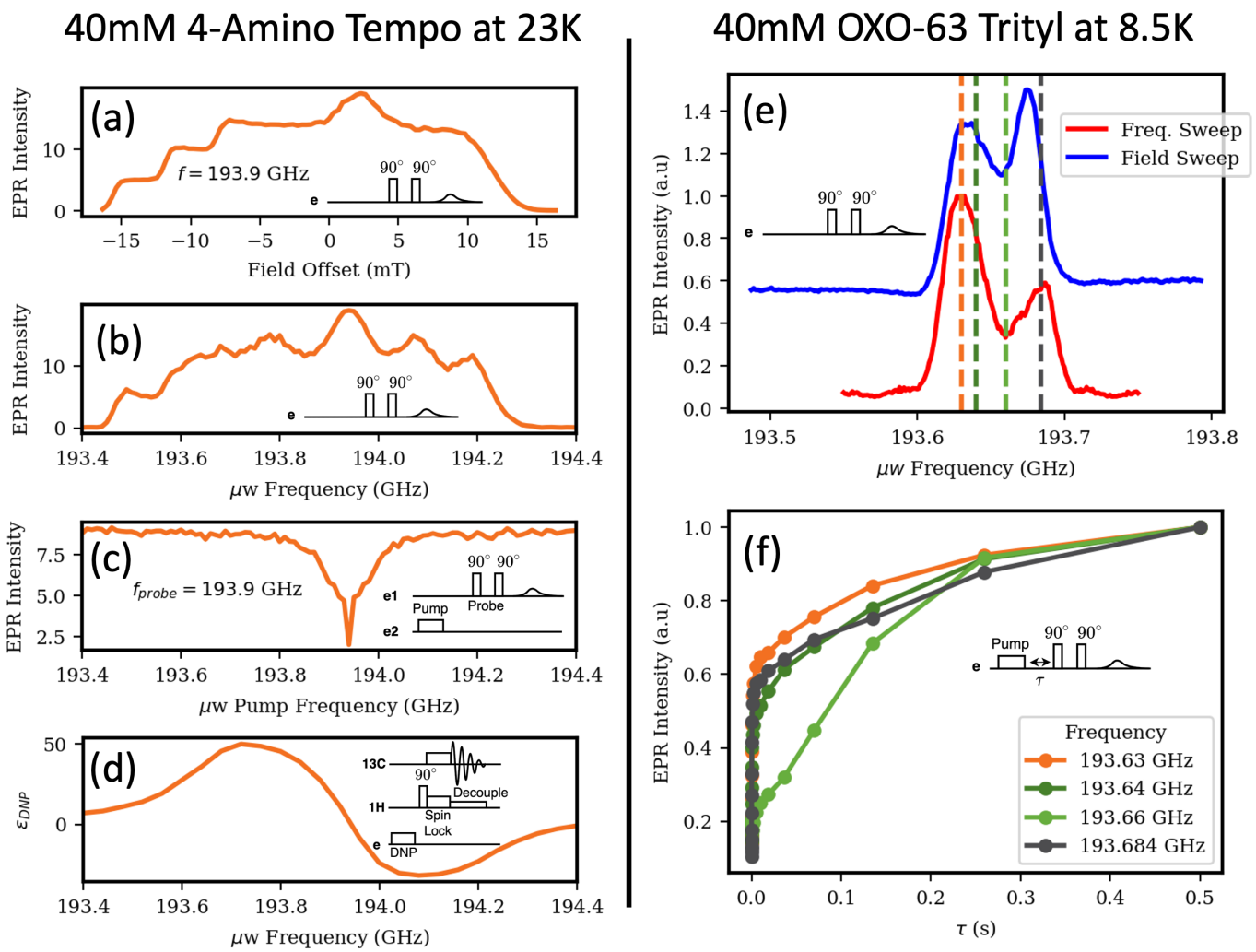

Figure 10: Left: EPR and DNP experiments on 4 amino tempo at 23K in DNP juice (60:30:10 d-glyercol, d2O, H2O). Inset are the pulse sequences used to acquire the data. (a) Field swept echo detected EPR spectra. (b) Frequency swept echo detected EPR spectra. Here we can see the effect of standing waves compared to the field swept spectra. (c) ELDOR profile. (d) 1H-13C CP DNP frequency profile with a 10s DNP buildup. Right: experiments on 40mM OXO-63 Trityl in DNP Juice at 8.5K. (e) Field and frequency swept echo detected EPR spectra. (f) Saturation recovery electron spin lattice relaxation measurements at different points on the EPR spectra.

DNP radicals. Underlying the design principle was the critical need to achieve affordable DNP/EPR operation under cryogenic temperature to make these studies less resource-limited.

While much optimization has been carried out on this dual EPR/DNP probe, there are still many ways this probe can be improved in terms of temperature, EPR and NMR performance, as suggested above. Furthermore, other practical improvements can be made to make the probe more versatile and operable. The "J arm" structure described above could be used as a sample exchange mechanism in which the entire probe is pulled from the cryostat for sample exchange without warming up the cryostat. Optical fibers can be installed to allow optical irradiation (and perhaps some detection) capabilities to the probe for Triplet DNP and other light-activated NMR, EPR or DNP experiments. ?

Acknowledgement

We would like to thank Dr. Ilia Kaminker for his insight into the μw mechanics involved in this work. We would also like to thank Dr. Asif Equbal for all his helpful discussions on applications of the dual EPR/DNP probe. This work was supported by the National Science Foundation Grant CHE CMI number 2004217. K.T. was partially supported by the Tokuyama Fellowship.

References

References

[1] D. A. Hall, D. C. Maus, G. J. Gerfen, S. J. Inati, L. R. Becerra, F. W. Dahlquist, R. G. Griffin, Polarization-enhanced NMR spectroscopy of biomolecules in frozen solution, Science 276 (5314) (1997) 930–932, ISSN 00368075.

[2] M. Afeworki, R. A. McKay, J. Schaefer, Selective Observation of the Interface of Heterogeneous Polycarbonate/Polystyrene Blends by Dynamic Nuclear Polarization Carbon-13 NMR Spectroscopy, Macromolecules 25 (16) (1992) 4084–4091, ISSN 15205835.

[3] R. A. Wind, J. Trommel, J. Smidt, Proton dynamic nuclear polarization in coal, Fuel 58 (12) (1979) 900–901, ISSN 0016-2361.

[4] M. Wang, X. P. Wu, S. Zheng, L. Zhao, L. Li, L. Shen, Y. Gao, N. Xue, X. Guo, W. Huang, Z. Gan, F. Blanc, Z. Yu, X. Ke, W. Ding, X. Q. Gong, C. P. Grey, L. Peng, Identification of different oxygen species in oxide nanostructures with 17O solid-state NMR spectroscopy, Science Advances 1 (1) (2015) e1400133, ISSN 23752548.

[5] M. E. Ward, L. S. Brown, V. Ladizhansky, Advanced solid-state NMR techniques for characterization of membrane protein structure and dynamics: Application to Anabaena Sensory Rhodopsin, Journal of Magnetic Resonance 253 (2015) 119–128, ISSN 10960856.

[6] T. Kobayashi, F. A. Perras, I. I. Slowing, A. D. Sadow, M. Pruski, Dynamic Nuclear Polarization Solid-State NMR in Heterogeneous Catalysis Research, 2015.

[7] A. Lesage, M. Lelli, D. Gajan, M. A. Caporini, V. Vitzthum, P. Miéville, J. Alauzun, A. Roussey, C. Thieuleux, A. Mehdi, G. Bodenhausen, C. Copéret, L. Emsley, Surface enhanced NMR spectroscopy by dynamic nuclear polarization, Journal of the American Chemical Society 132 (44) (2010) 15459–15461, ISSN 15205126.

[8] H. Takahashi, D. Lee, L. Dubois, M. Bardet, S. Hediger, G. Depaëpe, Rapid Natural-Abundance 2D 13C–13C Correlation Spectroscopy Using Dynamic Nuclear Polarization Enhanced Solid-State NMR and Matrix-Free Sample Preparation, Angewandte Chemie International Edition 51 (47) (2012) 11766–11769, ISSN 1521-3773.

[9] K. R. Thurber, R. Tycko, Theory for cross effect dynamic nuclear polarization under magic-angle spinning in solid state nuclear magnetic resonance: The importance of level crossings, Journal of Chemical Physics 137 (8) (2012) 084508, ISSN 00219606.

[10] F. Mentink-Vigier, Akbey, H. Oschkinat, S. Vega, A. Feintuch, Theoretical aspects of Magic Angle Spinning - Dynamic Nuclear Polarization, Journal of Magnetic Resonance 258 (2015) 102–120, ISSN 10960856.

[11] A. Zagdoun, G. Casano, O. Ouari, M. Schwarzwälder, A. J. Rossini, F. Aussenac, M. Yulikov, G. Jeschke, C. Copéret, A. Lesage, P. Tordo, L. Emsley, Large molecular weight nitroxide biradicals providing efficient dynamic nuclear polarization at temperatures up to 200 K, Journal of the American Chemical Society 135 (34) (2013) 12790–12797, ISSN 00027863.

[12] D. J. Kubicki, G. Casano, M. Schwarzwälder, S. Abel, C. Sauvée, K. Ganesan, M. Yulikov, A. J. Rossini, G. Jeschke, C. Copéret, A. Lesage, P. Tordo, O. Ouari, L. Emsley, Rational design of dinitroxide biradicals for efficient cross-effect dynamic nuclear polarization, Chemical Science 7 (1) (2016) 550–558, ISSN 20416539.

[13] J. Leggett, R. Hunter, J. Granwehr, R. Panek, A. J. Perez-Linde, A. J. Horsewill, J. McMaster, G. Smith, W. Köckenberger, A dedicated spectrometer for dissolution DNP NMR spectroscopy, Physical Chemistry Chemical Physics 12 (22) (2010) 5883–5892, ISSN 14639076.

[14] J. Granwehr, J. Leggett, W. Köckenberger, A low-cost implementation of EPR detection in a dissolution DNP setup, Journal of Magnetic Resonance 187 (2) (2007) 266–276, ISSN 10907807.

[15] A. A. Smith, B. Corzilius, J. A. Bryant, R. Derocher, P. P. Woskov, R. J. Temkin, R. G. Griffin, A 140 GHz pulsed EPR/212 MHz NMR spectrometer for DNP studies, Journal of Magnetic Resonance 223 (2012) 170–179, ISSN 10907807.

[16] A. Feintuch, D. Shimon, Y. Hovav, D. Banerjee, I. Kaminker, Y. Lipkin, K. Zibzener, B. Epel, S. Vega, D. Goldfarb, A Dynamic Nuclear Polarization spectrometer at 95 GHz/144 MHz with EPR and NMR excitation and detection capabilities, Journal of Magnetic Resonance 209 (2) (2011) 136–141, ISSN 10907807.

[17] T. A. Siaw, A. Leavesley, A. Lund, I. Kaminker, S. Han, A versatile and modular quasi optics-based 200 GHz dual dynamic nuclear polarization and electron paramagnetic resonance instrument, Journal of Magnetic Resonance 264 (2016) 131–153, ISSN 10907807.

[18] S. Takahashi, L. C. Brunel, D. T. Edwards, J. Van Tol, G. Ramian, S. Han, M. S. Sherwin, Pulsed electron paramagnetic resonance spectroscopy powered by a free-electron laser, Nature 2012 489:7416 489 (7416) (2012) 409–413, ISSN 1476-4687.

[19] J. H. Freed, New technologies in electron spin resonance, Annual Review of Physical Chemistry 51 (1) (2000) 655–689, ISSN 0066426X.

[20] R. Tycko, NMR at Low and Ultralow Temperatures, Accounts of Chemical Research 46 (9) (2013) 1923–1932.

[21] V. Aladin, B. Corzilius, Methyl dynamics in amino acids modulate heteronuclear cross relaxation in the solid state under MAS DNP, Solid State Nuclear Magnetic Resonance 99 (2019) 27–35, ISSN 09262040.

[22] A. H. Linden, W. T. Franks, Akbey, S. Lange, B. J. Van Rossum, H. Oschkinat, Cryogenic temperature effects and resolution upon slow cooling of protein preparations in solid state NMR, Journal of Biomolecular NMR 51 (3) (2011) 283–292, ISSN 09252738.

[23] Y. Matsuki, S. Nakamura, S. Fukui, H. Suematsu, T. Fujiwara, Closed-cycle cold helium magic-angle spinning for sensitivity-enhanced multidimensional solid-state NMR, Journal of Magnetic Resonance 259 (2015) 76–81, ISSN 1090-7807.

[24] Y. Li, R. Chaklashiya, H. Takahashi, Y. Kawahara, K. Tagami, C. Tobar, S. Han, Solid-state MAS NMR at ultra low temperature of hydrated alanine doped with DNP radicals, Journal of Magnetic Resonance 333 (2021) 107090, ISSN 1090-7807.

[25] K. Thurber, R. Tycko, Low-temperature dynamic nuclear polarization with helium-cooled samples and nitrogen-driven magic-angle spinning., Journal of magnetic resonance (San Diego, Calif. : 1997) 264 (2016) 99–106, ISSN 1096-0856.

[26] D. Lee, E. Bouleau, P. Saint-Bonnet, S. Hediger, G. De Paëpe, Ultralow temperature MAS-DNP, Journal of Magnetic Resonance 264 (2016) 116–124, ISSN 1090-7807.

[27] E. L. Sesti, N. Alaniva, P. W. Rand, E. J. Choi, B. J. Albert, E. P. Saliba, F. J. Scott, A. B. Barnes, Magic angle spinning NMR below 6K with a computational fluid dynamics analysis of fluid flow and temperature

gradients, Journal of Magnetic Resonance 286 (2018) 1–9, ISSN 1090-7807.
[28] P. Chen, B. J. Albert, C. Gao, N. Alaniva, L. E. Price, F. J. Scott, E. P. Saliba, E. L. Sesti, P. T. Judge, E. W. Fisher, A. B. Barnes, Magic angle spinning spheres, Science Advances 4 (9), ISSN 23752548.
[29] M. S. Conradi, Low-temperature NMR techniques, Concepts in Magnetic Resonance 5 (3) (1993) 243–262, ISSN 1099-0534.
[30] N. H. Balshaw, Practical Cryogenics: an introduction to laboratory cryogenics, 01865, ISBN 0 9527594 0 3, 2001.
[31] R. S. Khandpur, Cryostat, in: Compendium of Biomedical Instrumentation, Wiley, 561–565, 2020.
[32] D. Arčon, I. Heinmaa, R. Stern, Chapter 8: Low-temperature NMR: Techniques and Applications, in: New Developments in NMR, vol. 2018-January, Royal Society of Chemistry, ISBN 9781782624479, 233–261, 2018.
[33] T. Cheng, A. P. Gaunt, I. Marco-Rius, M. Gehrung, A. P. Chen, J. J. van der Klink, A. Comment, A multisample 7 T dynamic nuclear polarization polarizer for preclinical hyperpolarized MR, NMR in Biomedicine 33 (5) (2020) e4264, ISSN 10991492.
[34] R. Balzan, L. Fernandes, A. Comment, L. Pidial, B. Tavitian, P. R. Vasos, Dissolution dynamic nuclear polarization instrumentation for real-time enzymatic reaction rate measurements by NMR, Journal of Visualized Experiments 2016 (108), ISSN 1940087X.
[35] K. R. Thurber, W.-M. Yau, R. Tycko, Low-temperature dynamic nuclear polarization at 9.4T with a 30mW microwave source, Journal of Magnetic Resonance 204 (2) (2010) 303–313, ISSN 10907807.
[36] A. Comment, B. van den Brandt, K. Uffmann, F. Kurdzesau, S. Jannin, J. Konter, P. Hautle, W. Wenckebach, R. Gruetter, J. van der Klink, Design and performance of a DNP prepolarizer coupled to a rodent MRI scanner, Concepts in Magnetic Resonance Part B: Magnetic Resonance Engineering 31B (4) (2007) 255–269, ISSN 15525031.
[37] K. Kouřil, H. Kouřilová, S. Bartram, M. H. Levitt, B. Meier, Scalable dissolution-dynamic nuclear polarization with rapid transfer of a polarized solid, Nature Communications 10 (1) (2019) 1–6, ISSN 20411723.
[38] T. A. Siaw, M. Fehr, A. Lund, A. Latimer, S. A. Walker, D. T. Edwards, S. I. Han, Effect of electron spin dynamics on solid-state dynamic nuclear polarization performance, Physical Chemistry Chemical Physics 16 (35) (2014) 18694–18706, ISSN 14639076.
[39] J. H. Ardenkjær-Larsen, S. Bowen, J. R. Petersen, O. Rybalko, M. S. Vinding, M. Ullisch, N. C. Nielsen, Cryogen-free dissolution dynamic nuclear polarization polarizer operating at 3.35 T, 6.70 T, and 10.1 T, Magnetic Resonance in Medicine 81 (3) (2019) 2184–2194, ISSN 1522-2594.
[40] M. Baudin, B. Vuichoud, A. Bornet, G. Bodenhausen, S. Jannin, A cryogen-consumption-free system for dynamic nuclear polarization at 9.4T, Journal of Magnetic Resonance 294 (2018) 115–121, ISSN 10960856.
[41] A. Kiswandhi, P. Niedbalski, C. Parish, Q. Wang, L. Lumata, Assembly and performance of a 6.4 T cryogen-free dynamic nuclear polarization system, Magnetic Resonance in Chemistry 55 (9) (2017) 846–852, ISSN 07491581.
[42] V. Parma, Cryostat Design, Tech. Rep., ????
[43] D. I. Hoult, The NMR receiver: A description and analysis of design, 1978.
[44] F. D. Doty, Probe Design and Construction .
[45] F. D. Doty, Solid State NMR Probe Design .
[46] A. Webb, Magnetic Resonance Technology: Hardware and System Component Design, ISBN 978-1-78262-359-5, 2016.
[47] L. R. Becerra, G. J. Gerfen, B. F. Bellew, J. A. Bryant, D. A. Hall, S. J. Inati, R. T. Weber, S. Un, T. F. Prisner, A. E. McDermott, K. W. Fishbein, K. E. Kreischer, R. J. Temkin, D. J. Singel, R. G. Griffin, A Spectrometer for Dynamic Nuclear Polarization and Electron Paramagnetic Resonance at High Frequencies, Journal of Magnetic Resonance, Series A 117 (1) (1995) 28–40, ISSN 10641858.
[48] F. J. Scott, E. P. Saliba, B. J. Albert, N. Alaniva, E. L. Sesti, C. Gao, N. C. Golota, E. J. Choi, A. P. Jagtap, J. J. Wittmann, M. Eckardt, W. Harneit, B. Corzilius, S. Th. Sigurdsson, A. B. Barnes, Frequency-agile gyrotron for electron decoupling and pulsed dynamic nuclear polarization, Journal of Magnetic Resonance 289 (2018) 45–54, ISSN 10960856.
[49] M. L. Guy, L. Zhu, C. Ramanathan, Design and characterization of a W-band system for modulated DNP experiments, Journal of Magnetic Resonance 261 (2015) 11–18, ISSN 10960856.
[50] J. H. Walton, M. S. Conradi, Probe tuning adjustments-Need they be in the probe?, Journal of Magnetic Resonance (1969) 81 (3) (1989) 623–627, ISSN 00222364.
[51] F. D. Doty, R. R. Inners, P. D. Ellis, A multinuclear double-tuned probe for applications with solids or liquids utilizing lumped tuning elements, Journal of Magnetic Resonance (1969) 43 (3) (1981) 399–416, ISSN 00222364.
[52] H. Kovacs, D. Moskau, M. Spraul, Cryogenically cooled probes - A leap in NMR technology, 2005.
[53] J. Thoris, B. Leon, A. Dubois, J. C. Bobo, Dielectric breakdown of cold gaseous helium in large gaps, Cryogenics 10 (2) (1970) 147–149, ISSN 00112275.
[54] T. A. Siaw, S. A. Walker, B. D. Armstrong, S. I. Han, Inductively coupled NMR probe for versatile dynamic nuclear polarization operation at 7 T: Observation of 61 2% 1H polarization at 4 K, Journal of Magnetic Resonance 221 (2012) 5–10, ISSN 1090-7807.
[55] M. Decorps, P. Blondet, H. Reutenauer, J. P. Albrand, C. Remy, An inductively coupled, series-tuned NMR probe, Journal of Magnetic Resonance (1969) 65 (1) (1985) 100–109, ISSN 00222364.
[56] P. L. Kuhns, M. J. Lizak, S.-H. Lee, M. S. Conradi, Inductive Coupling and Tuning in NMR Probes; Applications, Tech. Rep., 1988.
[57] A. P. Zens, Using magnetic coupling to improve multiple resonance NMR probe circuits, Journal of Magnetic Resonance 316 (2020) 106741, ISSN 10960856.
[58] B. M. Wood, R. F. Code, High-performance cryogenic pulsed NMR spectrometer, Review of Scientific Instruments 52 (3) (1981) 386–390, ISSN 00346748.
[59] A. P. Reyes, H. N. Bachman, W. P. Halperin, Versatile 4 K nuclear magnetic resonance probe and cryogenic system for small-bore high-field Bitter magnets, Review of Scientific Instruments 68 (5) (1998) 2132, ISSN 0034-6748.
[60] A. S. Lipton, R. W. Heck, J. A. Sears, P. D. Ellis, Low temperature solid-state NMR experiments of half-integer quadrupolar nuclides: caveats and data analysis, Journal of Magnetic Resonance 168 (1) (2004) 66–74, ISSN 1090-7807.
[61] A. A. Nevzorov, S. Milikisiyants, A. N. Marek, A. I. Smirnov, Multi-resonant photonic band-gap/saddle coil DNP probehead for static solid state NMR of microliter volume samples, Journal of Magnetic Resonance 297 (2018) 113–123, ISSN 10960856.
[62] K. R. Thurber, W. M. Yau, R. Tycko, Low-temperature dynamic nuclear polarization at 9.4 T with a 30 mW microwave source, Journal of Magnetic Resonance 204 (2) (2010) 303–313, ISSN 10907807.
[63] D. W. Alderman, D. M. Grant, An efficient decoupler coil design which reduces heating in conductive samples in superconducting spectrometers, Journal of Magnetic Resonance (1969) 36 (3) (1979) 447–451, ISSN 00222364.
[64] David M Pozar, Microwave engineering, vol. 8, John Wiley & Sons, ISBN 9788578110796, 1989.
[65] W. B. Lynch, K. A. Earle, J. H. Freed, 1-mm wave ESR spectrometer, Review of Scientific Instruments 59 (8) (1988) 1345–1351, ISSN 00346748.
[66] G. M. Smith, J. C. Lesurf, R. H. Mitchell, P. C. Riedi, High performance MM-wave electron spin resonance spectrometer, in: IEEE MTT-S International Microwave Symposium Digest, vol. 3, IEEE, ISSN 0149645X, 1677–1680, 1995.
[67] P. P. Woskov, V. S. Bajaj, M. K. Hornstein, R. J. Temkin, R. G. Griffin, Corrugated waveguide and directional coupler for CW 250-GHz gyrotron DNP experiments, IEEE Transactions on Microwave Theory and Techniques 53 (6 I) (2005) 1863–1869, ISSN 00189480.
[68] T. Maly, J. R. Sirigiri, Simplified THz Instrumentation for High-Field DNP-NMR Spectroscopy, Applied Magnetic Resonance 43 (1-2) (2012) 181–194, ISSN 09379347.
[69] V. Weis, M. Bennati, M. Rosay, J. A. Bryant, R. G. Griffin, High-Field DNP and ENDOR with a Novel Multiple-Frequency Resonance Structure, Tech. Rep., 1999.
[70] V. Denysenkov, T. Prisner, Liquid state Dynamic Nuclear Polarization probe with Fabry-Perot resonator at 9.2 T, Journal of Magnetic Resonance 217 (2012) 1–5, ISSN 10960856.
[71] Y. Fuiiil, Y. Ishikawa, Y. Koizumi, T. Omija, I. Ohya, S. Mitsudo, S. Miura, H. Yamamori, H. Kikuchi, A. Fukuda, Development of

Millimeter-Wave Fabry-Perot Resonator for Simultaneous Electron-Spin and Nuclear-Magnetic Resonance Measurement at Low Temperatures, in: International Conference on Infrared, Millimeter, and Terahertz Waves, IRMMW-THz, vol. 2018-September, IEEE Computer Society, ISBN 9781538638095, ISSN 21622035, 2018.

[72] T. Prisner, V. Denysenkov, D. Sezer, Liquid state DNP at high magnetic fields: Instrumentation, experimental results and atomistic modelling by molecular dynamics simulations, Journal of Magnetic Resonance 264 (2016) 68–77, ISSN 10960856.

[73] J. Van Tol, L. C. Brunel, R. J. Wylde, A quasioptical transient electron spin resonance spectrometer operating at 120 and 240 GHz, Review of Scientific Instruments 76 (7) (2005) 074101, ISSN 00346748.

[74] O. Jakdetchai, V. Denysenkov, J. Becker-Baldus, B. Dutagaci, T. F. Prisner, C. Glaubitz, Dynamic nuclear polarization-enhanced NMR on aligned lipid bilayers at ambient temperature, Journal of the American Chemical Society 136 (44) (2014) 15533–15536, ISSN 15205126.

[75] K. O. Tan, C. Yang, R. T. Weber, G. Mathies, R. G. Griffin, Time-optimized pulsed dynamic nuclear polarization, Science Advances 5 (1) (2019) eaav6909, ISSN 23752548.

[76] E. J. Reijerse, High-frequency EPR instrumentation, Applied Magnetic Resonance 37 (1) (2010) 795–818, ISSN 09379347.

[77] F. H. Cho, V. Stepanov, S. Takahashi, A high-frequency electron paramagnetic resonance spectrometer for multi-dimensional, multi-frequency, and multi-phase pulsed measurements, Review of Scientific Instruments 85 (7) (2014) 075110, ISSN 10897623.

[78] J. P. Crenn, Optical propagation of the HE11 mode and Gaussian beams in hollow circular waveguides, International Journal of Infrared and Millimeter Waves 14 (10) (1993) 1947–1973, ISSN 01959271.

[79] J. W. Lamb, Miscellaneous data on materials for millimetre and submillimetre optics, International Journal of Infrared and Millimeter Waves 17 (12) (1996) 1997–2034, ISSN 01959271.

[80] B. D. Armstrong, D. T. Edwards, R. J. Wylde, S. A. Walker, S. Han, A 200 GHz dynamic nuclear polarization spectrometer, Physical Chemistry Chemical Physics 12 (22) (2010) 5920–5926, ISSN 1463-9084.

[81] S. A. Walker, D. T. Edwards, T. A. Siaw, B. D. Armstrong, S. Han, Temperature dependence of high field 13C dynamic nuclear polarization processes with trityl radicals below 35 Kelvin, Physical Chemistry Chemical Physics 15 (36) (2013) 15106–15120, ISSN 14639076.

[82] A. Lund, M. F. Hsieh, T. A. Siaw, S. I. Han, Direct dynamic nuclear polarization targeting catalytically active 27Al sites, Physical Chemistry Chemical Physics 17 (38) (2015) 25449–25454, ISSN 1463-9084.

[83] T. A. Siaw, A. Leavesley, A. Lund, I. Kaminker, S. Han, A versatile and modular quasi optics-based 200 GHz dual dynamic nuclear polarization and electron paramagnetic resonance instrument, Journal of Magnetic Resonance 264 (2016) 131–153, ISSN 10960856.

[84] I. Kaminker, R. Barnes, S. Han, Arbitrary waveform modulated pulse EPR at 200 GHz, Journal of Magnetic Resonance 279 (2017) 81–90, ISSN 10960856.

[85] D. H. Fabini, T. A. Siaw, C. C. Stoumpos, G. Laurita, D. Olds, K. Page, J. G. Hu, M. G. Kanatzidis, S. Han, R. Seshadri, Universal Dynamics of Molecular Reorientation in Hybrid Lead Iodide Perovskites, Journal of the American Chemical Society 139 (46) (2017) 16875–16884, ISSN 15205126.

[86] A. Lund, A. Equbal, S. Han, Tuning nuclear depolarization under MAS by electron T1e, Physical Chemistry Chemical Physics 20 (37) (2018) 23976–23987, ISSN 14639076.

[87] A. Leavesley, C. B. Wilson, M. Sherwin, S. Han, Effect of water/glycerol polymorphism on dynamic nuclear polarization, Physical Chemistry Chemical Physics 20 (15) (2018) 9897–9903, ISSN 14639076.

[88] A. Equbal, Y. Li, A. Leavesley, S. Huang, S. Rajca, A. Rajca, S. Han, Truncated Cross Effect Dynamic Nuclear Polarization: An Overhauser Effect Doppelgänger, Journal of Physical Chemistry Letters 9 (9) (2018) 2175–2180, ISSN 19487185.

[89] S. K. Jain, T. A. Siaw, A. Equbal, C. B. Wilson, I. Kaminker, S. Han, Reversal of Paramagnetic Effects by Electron Spin Saturation, Journal of Physical Chemistry C 122 (10) (2018) 5578–5589, ISSN 19327455.

[90] I. Kaminker, S. Han, Amplification of Dynamic Nuclear Polarization at 200 GHz by Arbitrary Pulse Shaping of the Electron Spin Saturation Profile, J. Phys. Chem. Lett 9 (2018) 44.

[91] A. Leavesley, S. Jain, I. Kamniker, H. Zhang, S. Rajca, A. Rajca, S. Han, Maximizing NMR signal per unit time by facilitating the e–e–n cross effect DNP rate, Physical Chemistry Chemical Physics 20 (43) (2018) 27646–27657, ISSN 1463-9084.

[92] A. Leavesley, I. Kaminker, S. Han, Versatile Dynamic Nuclear Polarization Hardware with Integrated Electron Paramagnetic Resonance Capabilities, eMagRes 7 (4) (2018) 133–154, ISSN 20556101.

[93] Y. Li, A. Equbal, K. Tagami, S. Han, Electron spin density matching for cross-effect dynamic nuclear polarization, Chemical Communications 55 (53) (2019) 7591–7594, ISSN 1364-548X.

[94] A. Equbal, S. K. Jain, Y. Li, K. Tagami, X. Wang, S. Han, Role of electron spin dynamics and coupling network in designing dynamic nuclear polarization, Progress in Nuclear Magnetic Resonance Spectroscopy 126-127 (2021) 1–16, ISSN 0079-6565.

[95] E. H. Williams, Magnetic Properties of Copper-Nickel Alloys, Physical Review 38 (4) (1931) 828, ISSN 0031899X.

[96] C. Lau, M. C. Kaufman, E. J. Doyle, G. R. Hanson, W. A. Peebles, G. Wang, A. Zolfaghari, Circular Corrugated Miter Bend and Gap Losses for Broadband Frequency Applications, IEEE Transactions on Microwave Theory and Techniques 67 (1) (2019) 38–49, ISSN 00189480.

[97] N. Simon, Cryogenic Properties of Inorganic Insulation Materials for ITER Magnets: A Review, Tech. Rep., Oak Ridge Operations, Oak Ridge, TN, 1994.

[98] F. Bonetto, E. Anoardo, M. Polello, Saddle coils for uniform static magnetic field generation in NMR experiments, Concepts in Magnetic Resonance Part B: Magnetic Resonance Engineering 29B (1) (2006) 9–19, ISSN 1552-5031.

[99] L. F. Fuks, W. Anderson, Perturbation Method for Finding the RF Field of an NMR Probe, 1997.

[100] A. Patel, R. Goswami, A. Vala, K. Mahant, H. Mewada, P. Bhatt, K. Sathyanarayan, S. V. Kulkarni, Millimeter-wave TE ¡sub¿01¡/sub¿ –TE ¡sub¿11¡/sub¿ –HE ¡sub¿11¡/sub¿ mode converter using overmoded circular waveguide, Journal of Electromagnetic Waves and Applications 32 (14) (2018) 1768–1778, ISSN 0920-5071.

[101] D. J. Kubicki, A. J. Rossini, A. Purea, A. Zagdoun, O. Ouari, P. Tordo, F. Engelke, A. Lesage, L. Emsley,